TECHNISCHE UNIVERSITÄT WIEN
Vienna University of Technology

D I P L O M A R B E I T

Synthesis and TEM investigation of $(Fe,Co)_{2-3}B$:
A compound for rare earth free permanent magnets

Ausgeführt am Institut für Festkörperphysik

der Technischen Universität Wien

unter der Anleitung von

Univ.-Prof. Dipl.-Ing. Dr.techn. Josef Fidler

durch

Wolfgang Wallisch, B.Sc.

Hackengasse 7/23

1150 Wien

_____   _____
            Datum   Unterschrift

Statutory Declaration

I herewith declare that I have authored this thesis independently and I have only used the declared sources/resources. I also declare that I have explicitly marked all materials which have been quoted either literally or by content from the used sources.

Vienna, 14.04.2015   Wolfgang Wallisch

Acknowledgement

"No one undertakes research in physics with the intention of winning a prize. It is the joy of discovering something no one knew before." - Stephen Hawking

Abstract

In the last years the enhanced research of alternatives to permanent magnets with rare earth elements has been strengthened by economic reasons and an increasing demand of permanent magnets. On the search for new magnetic materials, which are able to compete the current permanent rare earth magnets, Co and Fe containing binary and ternary compounds with a promising high magnetocrystalline anisotropy seems to be a substantial solution. $(Fe,Co)_{2-3}B$ based alloys are a potential candidate for novel hard magnetic applications in consequence of a high magnetocrystalline anisotropy constant of about $K_1 = 0.41$ MJ/m³.

This thesis describes the synthesis and the analysis of the phase relations in various microcrystalline alloys with a nominal composition of $(Fe_{1-x}Co_x)_{71}B_{29}$ ($0 \leq x \leq 1$). Initially, cast ingots have been synthesized by induction melting in inert atmosphere using master alloys. Furthermore, the ribbon casting process was realized with a melt-spinning facility and thereby the specimen got melted and were prepared with different wheel speeds of 18.9 m/s, 23.6 m/s, 26.7 m/s, 33 m/s and 37.7 m/s. Afterwards the melt-spun ribbons of selected compositions got a further heat treatment.

For the purpose of determining the magnetic properties the alloys were analysed at room temperature by vibrating sample magnetometer (VSM). To characterize the phase relations of selected alloys, a powder X-ray diffraction was used. The cast material and selected melt-spun ribbons were investigated by field emission gun scanning electron microscope (FEGSEM) to study the microstructure of the alloys. In addition, samples were prepared by conventional ion milling and subsequently analysed by using a transmission electron microscope (TEM).

The best hard magnetic properties were obtained for the $(Fe_{0.7}Co_{0.3})_{71}B_{29}$ alloy at 26.7 m/s.

Kurzfassung

Aufgrund einer zunehmenden Nachfrage nach Permanentmagneten und aus wirtschaftlichem Interesse wurde die Forschung nach Alternativen zu den Seltenerd-Permanentmagneten in den letzten Jahren intensiviert. Auf der Suche nach neuen magnetischen Materialien, welche im Stande sind mit den jetzigen Seltenerd-Permanentmagneten zu konkurrieren, erscheinen Co und Fe enthaltende binäre und ternäre Verbindung aufgrund ihrer hohen magnetokristallinen Anisotropie als vielversprechend. Auch $(Fe,Co)_{2-3}B$ Legierungen sind infolge einer hohen magnetokristallinen Anisotropiekonstante von $K_1 = 0.41$ MJ/m³ ein potentieller Kandidat für hart magnetische Anwendungen.

Das Ziel dieser Arbeit ist die Herstellung und Analyse der Phasenbeziehungen von verschiedenen mikrokristallinen Legierungen mit einer nominalen Zusammensetzung von $(Fe_{1-x}Co_x)_{71}B_{29}$ ($0 \leq x \leq 1$). Zuerst wurden die Gussbarren unter Verwendung einer Vorlegierung durch induktives Schmelzen in einer Schutzgasatmosphäre hergestellt. Mit Hilfe einer Melt-spinning Anlage konnten aus den Gussbarren Bänder gewonnen werden. Während dieses Prozesses wurde die Probe neuerlich erhitzt und bei unterschiedlichen Kupferradgeschwindigkeiten von 18.9 m/s, 23.6 m/s, 26.7 m/s, 33 m/s und 37.7 m/s erzeugt. Anschließend sind Bänder von ausgewählten Zusammensetzungen einer weiteren Wärmebehandlung unterzogen worden.

Zur Bestimmung der magnetischen Eigenschaften wurden die Legierungen bei Raumtemperatur mittels Vibrationsprobenmagnetometer untersucht. Für die Charakterisierung der Phasenbeziehungen ausgewählter Legierungen kam die Pulverdiffraktometrie zum Einsatz. Die Mikrostruktur des Gusswerkstoffes und einige Bänder wurden mit Hilfe des Feldemissionsrastermikroskops (FEGSEM) analysiert. Zusätzlich wurden Proben mittels konventionellen Ionenmühlen präpariert und anschließend mittels eines Transmissionselektronenmikroskops (TEM) untersucht.

Die besten hartmagnetischen Eigenschaften wurden für die $(Fe_{0.7}Co_{0.3})_{71}B_{29}$ Legierung bei 26.7 m/s erreicht.

Content

1

Introduction

The history of magnetism dates back for a long period of time and has fascinated the humanity from the very beginning. Magnetism is one of the most interesting phenomena, because humans are not able to perceive it with their five senses [1]. Thales of Miletus (624 - 546 B.C.) was one of the first, who described the properties of magnetic materials and the ancient Chinese took advantage of the particular power of lodestones by using a compass [1-3]. Due to its property of attracting iron, the first known magnetic material was the magnetite Fe_3O_4 [3, 4]. A lot of work had to be done and these days magnets are important in our everyday life and covering a wide variety of application, e.g. in automobiles, medical products, consumer electric products and many more. In general, this huge spectrum of application for magnetic materials enables magnets to be a part of almost all electronic and electrical devices. According to their coercivity, the magnetic materials are usually subdivided into permanent (hard) magnets ($H_c > 400$ kAm^{-1}), magnetic recording media (10 kAm$^{-1} < H_c < 400$ kAm^{-1}) and soft magnets ($H_c < 10$ kAm^{-1}) as shown in Fig. 1 [3]. The most common alloys of permanent magnets are $Ba_2Fe_{12}O_{19}$, $Sr_2Fe_{12}O_{19}$ and especially $Nd_2Fe_{14}B$ for permanent magnets containing rare earth elements. Typical representatives of soft magnets are Fe-Si alloys and for magnetic recording Fe–Ni, Fe–Co and Mn-based alloys are used [1].
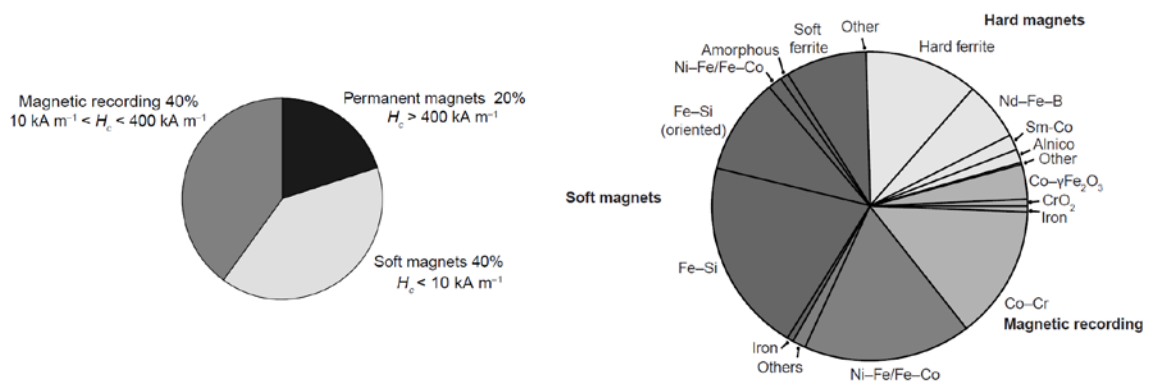
Fig. 1: Both circles exhibit an overview of magnets in the world market in 2009 [3]. The left circle provides a breakdown by the main distributions and the right circle is allocated to the known compositions.

The total circles symbolize the world market with an amount of 30 billion Dollar per year in 2009 and even high performance permanent magnets represent 20 % of the cake [3]. There are also other forecasts, which are based on different assumptions as different

parameters in the subdivision of magnetic materials and predict that the permanent magnet markets will increase prospectively from 11 billion in 2010 to 15.5 billion Dollars in 2020 [5].

The current research is concentrating on the development of stronger, lighter and more efficient magnetic materials [6]. The stronger a magnet is, the more efficient a device can operate. The main objective from the vantage point of the present is the improvement of the efficiency and performance of devices in all energy-use sectors of the economy. In recent times, the costs of rare earth have been considerably increased and on the basis of economic reasons more attention is given to the research of alternative hard magnetic materials, cost reduction and recycling [7]. The last years, an enhanced research of alternatives to permanent magnets containing rare earth elements were provided. The ambition to reduce or to replace the rare earth content is to find new magnetic materials, which are able to compete the current high performing permanent magnet devices. The preparation of modern magnets is based on enhanced microstructure, which can include precipitates, defects etc. and compounds with crucial intrinsic properties. A permanent magnet has to fulfil several physical characteristics, such as coercivity, high magnetocrystalline anisotropy and/or shape anisotropy, respectively. In addition, an adequate large saturation polarization is necessary for the purpose of achieving a high energy density product. Nevertheless, to enable a broad scope of application the Curie temperature should be sufficient high. The optimization of the extrinsic material parameters, as the microstructure, consists of amorphous regions and the right constellation of small and/or large magnetic grains, for example [8].
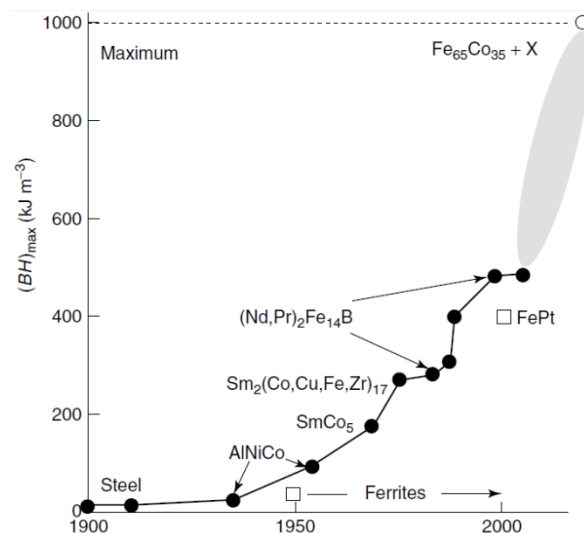
Fig. 2: The development of hard magnets over the last years with a forecast of new magnetic materials (shaded area) is shown by Goll [8].

These properties can be assessed by an appropriate choice of the alloy composition taken from the phase diagram and by the processing methods as sintering, rapid-solidification, quenching, chemical synthesis etc. [8]. The development of the maximum energy density product $(BH)_{max}$ over the last hundred years is presented by Goll [8] in Fig. 2. The diagram shows the progress of hard magnetic materials and the forecast (shaded area) of new permanent magnets, which could be achieved by FeCo based alloys in the future. The research into new magnetic materials with a high magnetocrystalline anisotropy for the replacement of rare earth permanent magnet materials leads to Fe and Co containing binary and ternary compounds [9]. As illustrated in Fig. 3, $(Fe,Co)_{2-3}B$ based alloys exhibit a potential as basis for novel hard magnetic applications.

Fig. 3: Illustration of the temperature dependence of magnetocrystalline anisotropy constant K_1. The red circle marks the compound $(Fe_{0.7}Co_{0.3})_2B$ with K1 = 400 kJm^{-3}, M ~160 emu/ g and $H_{C, max}$ ~0.5T [10].

In 1970, a series of $(Fe_{1-x}Co_x)_2B$ ($0 \leq x \leq 1$) compounds was analysed by Iga [10] with magnetic torque experiments on single crystals. The parent binaries, Co_2B and Fe_2B,

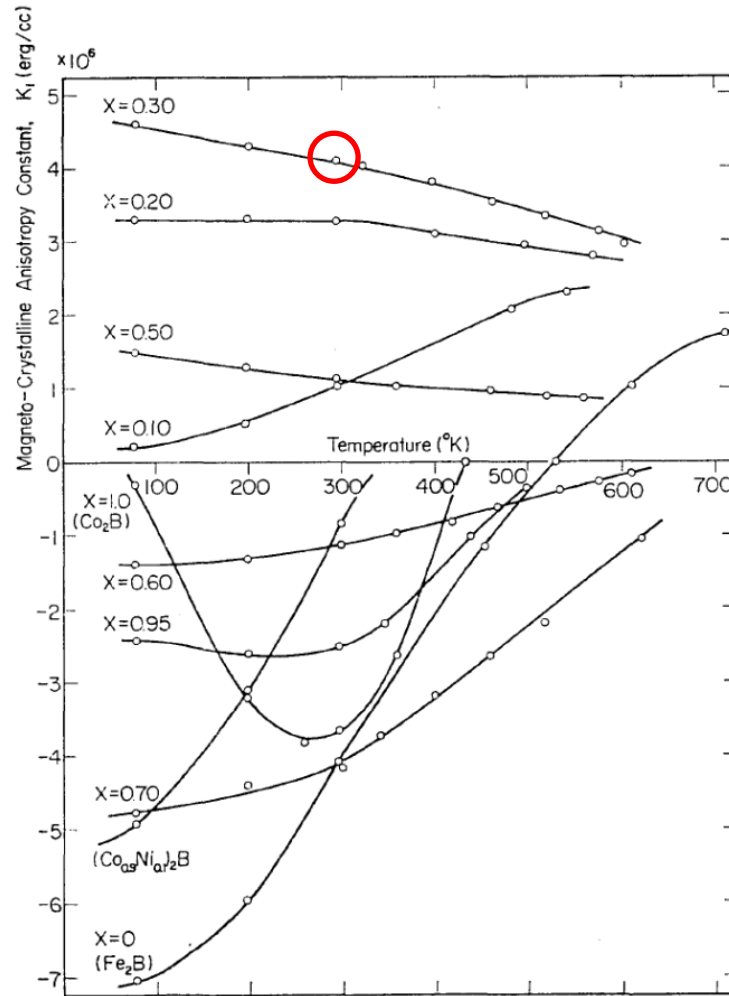exhibit an easy-plane anisotropy, whereas in the range of $0.1 < x < 0.5$ an easy–axis anisotropy was measured. The maximum value of the magnetocrystalline anisotropy constant $K_1 = 410$ kJ/m³ has been measured for the $(Fe_{0.7}Co_{0.3})_2B$ alloy at room temperature and is marked with a red circle in Fig. 3. Furthermore, in 1975 Takacs [11] was also investigating the intermetallic compounds $(Fe_{1-x}Co_x)_2B$ and $(Fe_{1-x}Co_x)B$ by Mössbauer spectroscopy and reported an increasing magnetic moment of cobalt, while the cobalt content is decreasing. In contrast to this confirmation, the iron moment is more or less unchanged during the variation of the concentration x in $(Fe_{1-x}Co_x)_2B$ alloys. The occurrence is possibly based on the hybridization change of the cobalt 3d and boron sp electrons by the Co concentration [11].

In 1991, Coene et al. [12] analysed the magnetocrystalline anisotropy of Fe_2B, Fe_3B and $Fe_{1.4}Co_{0.6}B$ compounds by Singular Point Detection experiments and Lorentz electron microscopy. The following measured anisotropy field values were obtained: $\mu_0H_a = 0.77$ T for $Fe_{1.4}Co_{0.6}B$, $\mu_0H_a = -0.4$ T for Fe_2B and $\mu_0H_a = -0.5$ T for Fe_3B. The negative value of H_a is attributed to an in-plane anisotropy, which is in accordance with the sign of K_1.

The study of Kuz'min et al. [13] confirmed the results of Iga [10] in 2014 and was focused on single crystal investigations in the easy-axis range of the $(Fe_{1-x}Co_x)_2B$ ($0 \leq x \leq 1$) compounds, thereby a magnetocrystalline anisotropy of $K_1 = 510$ kJ/m³ was obtained at low temperatures (0 K).

Based on these results, Jian et al. [14] examined the magnetic properties of $(Fe_{1-x}Co_x)_2B$ (x = 0.20, 0.25, 0.30, 0.35) alloys on single crystals in the temperature range from 10 to 1000 K in 2014. An easy-axis anisotropy of $K_1 = 450$ kJ/m^3 and a saturation magnetization of $M_S = 148$ Am^2/kg was achieved for $(Fe_{0.75}Co_{0.25})_2B$ at room temperature.

In 2015, Belashchenko et al. [15] published first-principles electronic structure investigations and showed by obtaining the optimal band filling with epitaxial strain or suitable chemical doping that the maximum concentration is x = 0.3. The consecutive filling of minority-spin electronic bands of particular orbital character and the associated spin-orbital selection rules determine the concentration value.

$(Fe_{1-x}Co_x)_2B$ alloys also were investigated experimentally and theoretically by Edström et al. [16] in 2015. A maximum of the magnetocrystalline anisotropy was shown at x = 0.3 by full-potential density functional theory (DFT) simulations and this result is in accordance with the saturation magnetization. The outcome of Edström [16] confirmed the result of Belashchenko [15].

Based on these findings, the motivation of this thesis is to find a potential candidate for novel hard magnetic application without containing rare earth elements. Due to the high

magnetocrystalline anisotropy of about $K_1 > 0.4$ MJ/m³, (Fe,Co)$_{2-3}$B based alloys are a promising permanent magnet replacement material. Thus, this work is focused on the synthesis, the microstructural and magnetic analysis of (Fe$_{1-x}$Co$_x$)$_{2-3}$B ($0 \leq x \leq 1$) alloys.

The thesis is structured as followed: In chapter 2 the relevant requirements for permanent magnets in this work are summarized. The material compositions and the synthesis by induction melting, melt-spinning and annealing are discussed in chapter 3. In the following chapter 4 the measurement methods and their results are presented. Chapter 5 gives an overview of the microcrystalline microstructure of the studied alloys. Finally, in chapter 6 the main results are discussed and afterwards a review with a short outlook is given.

2

Fundamental Requirements for Permanent Magnets

The following chapter gives an introduction into the requirements for permanent magnets, which is a necessary precondition for the understanding of the used measuring methods, the evaluation of the measurement data as well as the interpretation of the collected results.

2.1. Magnetic Hysteresis

The behaviour of magnetic materials preoccupies us since a long time and is accurately reflected in the hysteresis loop, which is the core and source of any further investigations as well as new technological progress [17]. The hysteresis loop is a significant magnetically fingerprint of the material and describes the magnetic properties of the studied specimen.
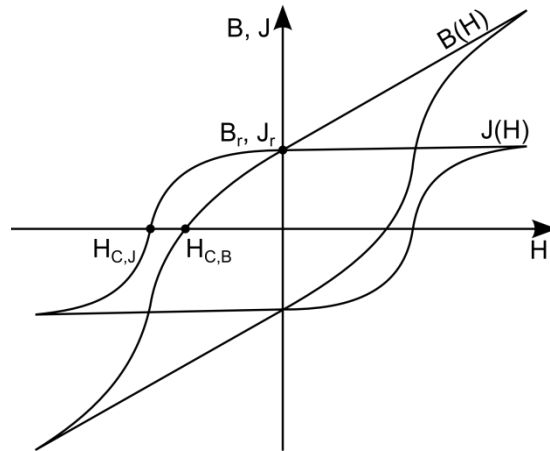
Fig. 4: Illustration of two hysteresis loops J(H) and B(H).

The hysteresis loop J(H), which is illustrated in Fig. 4, is the consequence of applying an external magnetic field H to the demagnetized specimen and measuring simultaneously the response of the magnetization M or the magnetic polarization

$$\vec{J} = \mu_0 \vec{M} \quad , \tag{1}$$

where $\mu_0 = 4\pi \cdot 10^{-7} \, \text{VsA}^{-1}\text{m}^{-1}$ is the vacuum permeability. Another possibility to illustrate the hysteresis loop is to apply the flux density over the external applied field $\mu_0 H$.

This relation between the polarization and the induction is represented by the following formula

$$\vec{B}(H) = \mu_0(\vec{H} + \vec{M}) = \mu_0\vec{H} + \vec{J} \tag{2}$$

and shown in Fig. 4 as hysteresis loop B(H). The choice of the right hysteresis description depends on the examination purpose. The J(H) loop gives a better reflection of the intrinsic properties, whereas the B(H) loop describes the behaviour of the working conditions [17]. An advantage of the B-H diagram is that the maximum energy density product $(BH)_{max}$ can be gained directly from the loop.

In general, a magnetic material consists of many magnetic moments, for example iron has a magnetic moment m of 2.2 μ_B per atom [1]. The atomic unit of magnetic moment is the Bohr magneton as related to

$$\mu_B = \frac{h \cdot q_e}{4 \cdot \pi \cdot m_e} \cong 9.27 \cdot 10^{-24} \ \text{Am}^2 \tag{3}$$

with the Planck's constant h, the electron charge q_e and the electron mass m_e. The individual grains of polycrystalline materials and their magnetic moment vectors m_i are randomly orientated and do not interact with each other, which leads to a macroscopic demagnetization. The process of the hysteresis loop starts at the demagnetized state (H = J = B = 0 T). By an external field, the polarization rises and the virgin curve develops as illustrated in Fig. 5. As a consequence of the application of an external field, the domain walls are first reversible displaced, but in the next step with an increase of the external field the domain walls are displaced irreversible. Finally, with a further increase of the applied field the direction of magnetization is rotating in every domain. Thus, the direction of the magnetization and the domain wall displacements are related to the initial permeability μ_i.
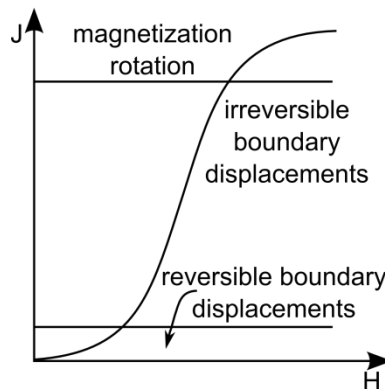

Fig. 5: Overview of the acting processes in the virgin curve [18].

On the way to the saturation polarization the applied field is further increasing and a growing number of domain walls changes the state from the original pinning to the next stronger pinning state. The reversible boundary displacements are switching to irreversible and finally at a very high field the domain motion is completed and the saturation polarization J_s or an asymptotic value of the flux density field is achieved.

After saturation the applied field is reduced to zero, the material begins to reverse its alignment and the magnetization attains the remanent state. The polarization at H = 0 is named as remanent polarization J_r. If a reversal magnetic field strength H_c, known as the coercive field, is applied, the remanent polarization goes down to zero. The negative saturation polarization $-J_s$ is achieved by increasing the reversed applied field -H. The hysteresis cycle is closed, if a positive field H is applied again and the right branch of the loop is passed as shown in Fig. 4.

2.2. Curie temperature T_c

The Curie temperature is an important point for today's applications, because the magnetic behaviour depends on this property. At the Curie temperature T_c the spontaneous magnetization of the Weiss domains goes down to zero (Fig. 6). The reason for this phenomenon is the temperature dependence of the magnetic moment alignment. Below T_c the properties of magnetic materials are ferromagnetic and above T_c the properties change to a paramagnetic behaviour.
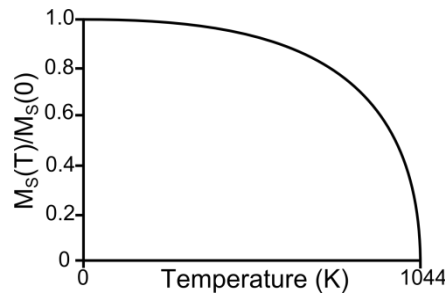

Fig. 6: Temperature dependence of Fe with its Curie temperature at 1044 K.

On the basis of this behaviour, Fig. 6 illustrates the dependence of the normalized magnetization from the temperature and exhibits that the Curie temperature has considerable significance by the right choice of magnetic materials for application.

2.3. Anisotropy

The natural direction of magnetization in ferro-, ferri- and antiferromagnetic materials lies along one or more preferred directions, so called easy axis. Strong easy axis anisotropy is assigned to the hard magnets and the weak hard axis anisotropy is attributed to soft magnets. The magnetic anisotropy affects the shape of the hysteresis loop and depends on the orbital-moment formation, the magnetoelasticity and the magnetoresistance [19]. The main sources of anisotropy are the magnetocrystalline anisotropy and the shape anisotropy.

Magnetocrystalline Anisotropy

The magnetocrystalline anisotropy is an intrinsic property, which depends on the crystal symmetry and its origin lies in the crystal-field interaction, the spin-orbit coupling or the interatomic dipole-dipole interaction. For example, typical values for anisotropy-energy densities are 0.05 MJ/m³ for bcc Fe, 0.5 MJ/m³ for hcp Co and as comparison 10 MJ/m³ for rare earth magnets. In total, the large spin-orbit coupling of the rare earth 4f electrons is responsible for this results [19].
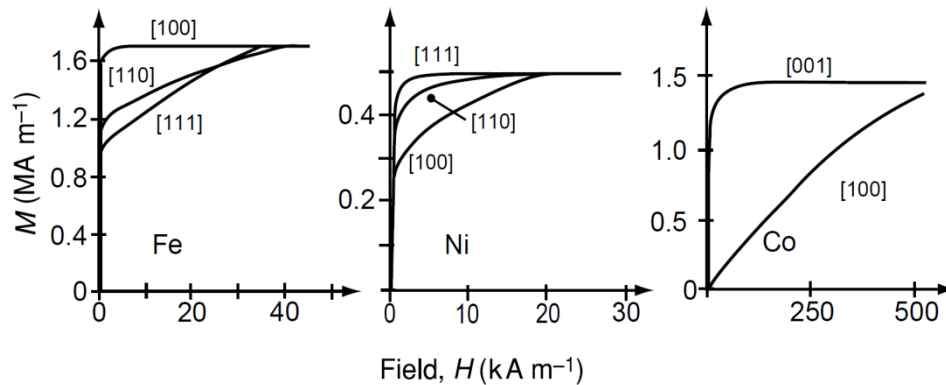
Fig. 7: Magnetization of single crystals of iron, nickel and cobalt according to [3].

Concerning this property, in Fig. 7 the magnetization curve of single crystals exhibits different directions of saturation and each specimen has a different easy and hard direction. Cobalt presents a unique easy axis direction and consequently uniaxial anisotropy, which is an essential precondition for permanent magnetism. A first-order approximation for the magnetization located along an easy axis is shown by the anisotropic energy

$$E_a = K_1 V \cdot sin^2\theta \quad , \tag{4}$$

whereas K_1 is the first- or second-order uniaxial anisotropy constant, V is the volume of the magnet and θ is the angle between the anisotropy axis and the magnetization. For magnets with uniaxial structure the angle between the anisotropy axis and the magnetization equals zero, which means that the symmetry axis corresponds to the

crystallographic c-axis [19]. In the case of polycrystalline magnets the term $K_1 sin^2\theta$ has to be replaced by

$$\frac{-K_1(n \cdot M)^2}{M_S^2} \quad , \tag{5}$$

where n is the spatially varying symmetry axis. Different expressions of the symmetry are given for the anisotropy-energy density E_a:

uniaxial anisotropy

$$\frac{E_a}{V} = K_1 sin^2\theta + K_2 sin^4\theta + K_3 sin^6\theta \tag{6}$$

tetragonal anisotropy

$$\frac{E_a}{V} = K_1 sin^2\theta + K_2 sin^4\theta + K'_2 sin^4\theta \cdot cos4\varphi + K_3 sin^6\theta + K'_3 sin^6\theta \cdot sin4\varphi \tag{7}$$

hexagonal and rhombohedral anisotropy

$$\frac{E_a}{V} = K_1 sin^2\theta + K_2 sin^4\theta + K_3 sin^6\theta + K'_3 sin^6\theta \cdot sin6\varphi \tag{8}$$

cubic anisotropy

$$\frac{E_a}{V} = K_1\left(s_x^2 s_y^2 + s_y^2 s_z^2 + s_z^2 s_x^2\right) + K_2(s_x^2 s_y^2 s_z^2) \tag{9}$$

These expressions don't include odd-order terms (for example: $sin\,\theta, sin^3\theta$). The preference of tetragonal, hexagonal or rhombohedral to cubic structures for permanent magnets and recording media is attributable to the smallness of the cubic anisotropy.

The field, which achieves the saturation of the magnetization, is called the anisotropy field H_a and for uniaxial magnets or cubic magnets with $K_1 > 0$ the following expression

$$H_a = \frac{2K_1}{J_S} \tag{10}$$

is applied. The definition of H_a is not so trivial for higher-order anisotropies and in the case of $K_1 < 0$ a new expression is given

$$H_a = -\frac{4K_1}{3J_S} \quad . \tag{11}$$

Shape Anisotropy

The shape anisotropy depends on the shape of the specimen as well as internal precipitates and therefore it is an extrinsic property. The direction, in which it comes to a minimization of the stray field or the demagnetization factor, is the easy axis of the shape anisotropy. The magnetostatic interaction energy E_{ms} of a pair of magnetic dipoles $m_{i/j}$ [19] is the foundation of the dipolar and the shape anisotropy

$$E_{ms}(i,j) = -\frac{1}{4\pi\mu_0} \frac{3m_i \cdot R_{ij}m_j \cdot R_{ij} - m_i \cdot m_j R_{ij}^2}{R_{ij}^5} \tag{12}$$

with μ_0 is the vacuum permeability, r_i and r_j are the position vectors of the magnetic dipoles and $R_{ij} = r_i - r_j$ is the relation between r_i and r_j. Due to simplification the summation over atomic dipole pairs is replaced by an integral and the following Equation (13) shows the transition from the discrete to continuous values

$$\sum_i \ldots m_i = \int \ldots M(r) \cdot dV \quad , \tag{13}$$

where M(r) is the magnetization. This leads to new expression of the total magnetostatic energy

$$E_{ms} = \frac{1}{2}\mu_0 \int M(r) \cdot H_D(r) \cdot dV \quad , \tag{14}$$

where H_D is the demagnetizing field strength. A brief examination of this term is given below.

Demagnetizing field strength H_D

Electric currents or magnetic poles can construct a magnetic field H [20]. In the case of electric currents the lines of the magnetic field are continuous and closed loops. For magnetic poles the field lines arise from them, their origin lies on the North Pole and ends on the South Pole. The demagnetization field H_D inside the material spreads from the north to the South Pole and is operating in the opposite direction of M. The relation between H_D and M is given by

$$H_D = -N \cdot M \quad , \tag{15}$$

where N is the demagnetization factor (or tensor) and its value is between $0 < N < 1$. The demagnetization factor N depends on the dimension (e.g. geometry) of the specimen.

The internal field H_i in the sample is the result of the interaction between the external field H_e and the demagnetization field H_D.

$$H_i = H_e + H_D = H_e - N \cdot M \tag{16}$$

It should be taken into account, that the magnetization is independent of the demagnetization field. This is the reason why highly anisotropic permanent magnets have a significant magnetization and the coercivity is greater than the demagnetization field [3].

Returning to Eq. (14) of the total magnetostatic energy, the expression of E_{ms} is simplified by considering a homogeneously magnetized ellipsoid

$$E_{ms} = \frac{J_s^2}{2\mu_0}\left(N_x s_x^2 + N_y s_y^2 + N_z s_z^2\right)V \quad, \tag{17}$$

where x, y and z are the principal axes of the ellipsoid, s_x, s_y, s_z are the direction cosines and N_x, N_y and N_z are the principal directions of the demagnetization factor.

The consideration of the uniaxial case of a prolate ellipsoid gives following relations, as $N_x = N_y$, $s_x^2 + s_y^2 + s_z^2 = 1$ and with $N_x + N_y + N_z = 1$ arises $N_z = 1 - 2N_x$. By using these formulations Equation (15) can be rewritten into

$$E_{ms} = \frac{J_s^2}{2\mu_0}(1 - 3N)V \tag{18}$$

and thus the shape anisotropy K_{sh}, a contribution of K_1, is obtained:

$$K_{sh} = \frac{J_s^2}{2\mu_0}(1 - 3N) \quad. \tag{19}$$

Differences of microcrystalline anisotropy and shape anisotropy

The consequences of the microcrystalline anisotropy and the shape anisotropy on magnetic materials are shown in the evaluation of micromagnetic modelling approaches for single high-aspect-nanostructures. The following micromagnetic simulations are based on the finite element method and were done by Finite Element MicroMagnEtics (FEMME) [21], which is able to calculate the body, regardless of the shape and the material. Therefore the contributions of the coercive field, which are affected by the microcrystalline anisotropy and the shape of the nanorods, can be measured qualitatively.

The materials with the following intrinsic properties (microcrystalline anisotropy constants K_1 and K_2, saturation polarization J_s, exchange constant A and Gilbert's damping coefficient), which were utilized for the simulations, are an uniaxial cobalt, a cubic iron and a cubic cobalt-iron as shown in Table 1.

Table 1: Intrinsic properties of the used materials.

Material	J_s (T)	A (J/m)	K_1 (J/m³)	K_2 (J/m³)	α
Co	1.76	$1.3 \cdot 10^{-11}$	$4.5 \cdot 10^5$		1.00
Fe	2.15	$2.5 \cdot 10^{-11}$	$4.6 \cdot 10^4$	$1.5 \cdot 10^4$	1.00
$Co_{50}Fe_{50}$	2.45	$1.3 \cdot 10^{-11}$	$-1.5 \cdot 10^4$	$-1.0 \cdot 10^2$	1.00

Real nanorods have circular diameters, however, to calculate such a nanorod model is complicated and extremely time-consuming, as the mesh for the simulation is already complex. Therefore an octagonal prism was chosen for the micromagnetic simulations. Three models with different diameters D (20 nm, 40 nm and 60 nm) and a constant height H of 400 nm were created.
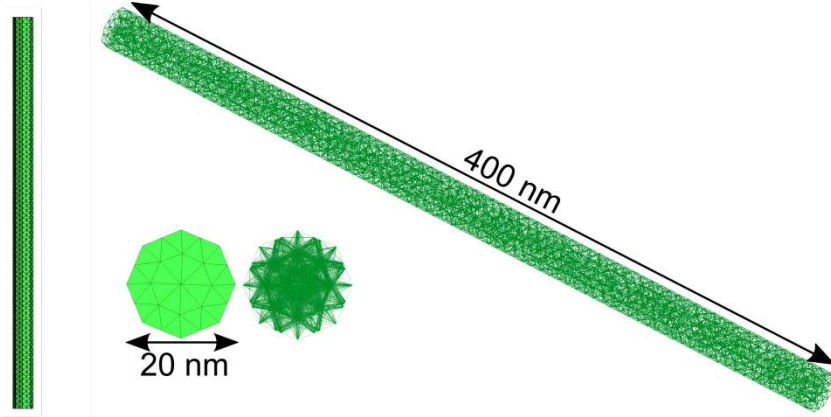

Fig. 8: Illustration of the surface mesh (right) and the mesh of the nanorods (left).

The investigated models were created with a mesh size of 5 nm by GiD 9.3.1b [22], which is a pre and postprocessor for numerical simulations, as shown in Fig. 8. The hysteresis loop started in the positive saturation of 1.5 T in z-direction (001) and the external field was applied in the opposite direction (00-1) to -1.5 T. After saturation the field was set in the opposite direction to reach the initial state of 1.5 T. A field rate of 0.01 T/ns was chosen for the hysteresis loop. In order to obviate any difficulties during the calculations due to the perfect congruence, the direction of the external field was tilted 0.1 rad off-axis for the Co- and Fe-models, and for the $Co_{50}Fe_{50}$-model the tilt of 0.1 rad was done in each direction.
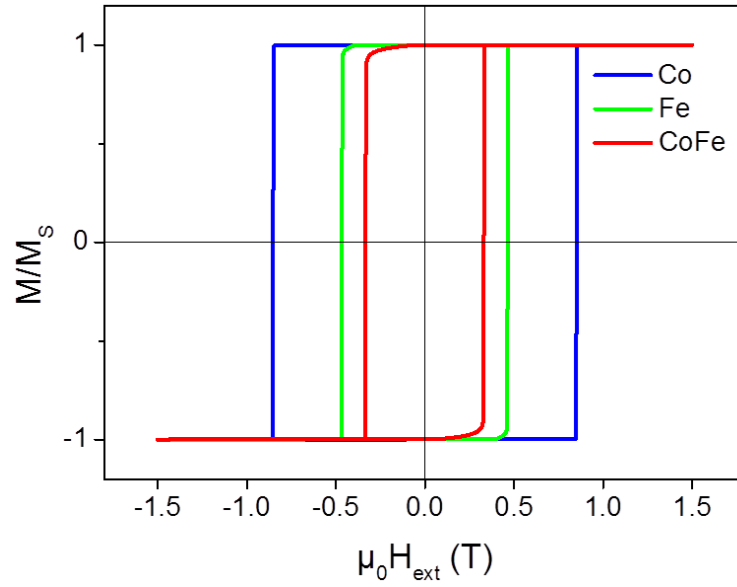
Fig. 9: Hysteresis loops of nanorods with an aspect ratio H/D of 20.

It could be observed that with constant diameter and constant height the coercive filed depends on the intrinsic properties of the materials (Fig. 9), which is attributed to the microcrystalline anisotropy.
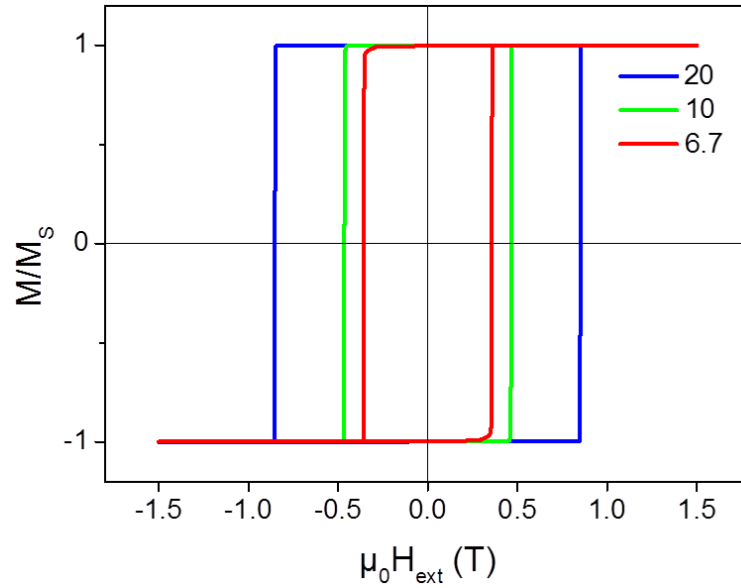

Fig. 10: Hysteresis loops of Co with different aspect ratios H/D. The highest aspect ratio achieves the highest coercivity of 0.852 T.

The growth of the aspect ratio H/D shown in Fig. 10 leads to an increase of H_c, which is affected by the shape anisotropy.

2.4 Susceptibility χ and Permeability μ

The susceptibility of the material χ is a dimensionless scalar and is defined as

$$\chi = {}^{M}/_{H} \quad . \tag{20}$$

There is also a possibility to express the susceptibility with the relation between the susceptibility and the relative permeability μ_r is given by

$$\chi = \mu_r - 1 \quad . \tag{21}$$

By means of Eqs. (20) to (21) the following Equation can be written as

$$B = \mu_0 \cdot (H + M) = \mu_0 \cdot \mu_r \cdot H \quad . \tag{22}$$

As a consequence the absolute permeability μ is determined by the ratio of the magnetic flux density B to the field strength H

$$\mu = {}^{B}/_{H} \quad , \tag{23}$$

whereby the absolute permeability consists of the relative permeability μ_r and the magnetic constant μ_0

$$\mu = \mu_r \cdot \mu_0 \quad . \tag{24}$$

Usually the relative permeability μ_r is used for the characterization of magnetic materials. The relative permeability μ_r can be derived from Eq. (22)

$$\mu_r = \frac{B}{\mu_0 \cdot H} = 1 + \frac{J}{\mu_0 \cdot H} \quad . \tag{25}$$

Under the assumption the permeability is constant, which is in the linear range of the flat hysteresis curve and the knowledge of the anisotropy field strength H_a in Eq. (10), Eq. (25) can be written as

$$\mu_r = 1 + \frac{J_s}{\mu_0 \cdot H_a} = 1 + \frac{J_s^2}{2 \cdot \mu_0 \cdot K_1} \cong \frac{J_s^2}{2 \cdot \mu_0 \cdot K_1} \quad . \tag{26}$$

This equation supplies the relation between the permeability and the anisotropy constant.

2.5. Coercive field H$_c$

The coercive field or coercivity is the measured field strength that is able to reverse the magnetization of the magnetic material. For the purpose of the coercive field derivation,

the simple case of a Stoner-Wohlfarth particle with its easy axis parallel to the z-axis is considered and the total energy density [23] is

$$\frac{E}{V} = K_1 sin^2\theta + K_2 sin^4\theta + \frac{\mu_0}{2}(1 - 3N)M_s^2 sin^2\theta + \mu_0 M_s H_{ext} cos(\varphi_0 + \theta) \quad , \qquad (27)$$

where θ is the angle between the magnetization and the direction of the external field. The vanishing derivation dE/dθ = 0 (Eq. 28) and the second derivation d²E/dθ² ≤ 0 (Eq. 29) are conditions for the spontaneous rotation of M_s into the opposite direction.

$$\frac{1}{V}\frac{dE}{d\theta} = (K_1 + \frac{\mu_0(1 - 3N)M_s^2}{2})sin2\theta + 2K_2 sin^2\theta sin2\theta - \mu_0 M_s H_{ext} sin(\varphi_0 + \theta) \qquad (28)$$

$$\frac{1}{V}\frac{d^2E}{d\theta^2} = 2(K_1 + \frac{\mu_0(1 - 3N)M_s^2}{2})cos2\theta + 4K_2(3cos^2 - sin^4\theta) - \mu_0 M_s H_{ext} cos(\varphi_0 + \theta) \leq 0 \quad (29)$$

By means of linearization the nucleation field for $\varphi_0 = 0$ follows from Eq. (28) [23]

$$\left[2\left(K_1 + \frac{\mu_0}{2}(1 - 3N)M_s^2\right) - \mu_0 M_s H_{ext}\right]\theta = 0 \quad . \qquad (30)$$

Due to the independence of the nucleation field form the particle and K_2, the corresponding coercivity is

$$H_c = \frac{2K_1}{\mu_0 M_s} + (1 - 3N)M_s \quad . \qquad (31)$$

In the case of a sphere (N = 1/3) Eq. (31) allows a simple approximation of the coercive field

$$H_c = \frac{2K_1}{Js} \quad . \qquad (32)$$

2.6. Saturation Polarisation J$_s$

If the magnetic moments are completely orientated parallel to the external field, the magnetic material is saturated. In the case that all magnetic domains are orientated in the external field direction, it could be possible that with a further increase of the field strength a slow rise of the spontaneous magnetization is achieved.

The law of approach to saturation (LAS) describes the magnetization curve near the saturation as a function of the magnetic field:

$$M = M_s\left(1 - \frac{a}{H} - \frac{b}{H^2} - \dots\right) + \chi_0 H \quad , \qquad (33)$$

whereas M is the magnetization, M_s is the saturation magnetization, $\frac{a}{H}$ is the inhomogeneity term of the material (e. g. defects), $\frac{b}{H^2}$ is proportional to the magnetic anisotropy and the last term $\chi_0 H$ reflects the high-field susceptibility.

2.7. Energy density product (BH)$_{max}$

The maximum energy density product of a magnetic material can be directly attained out of the B-H hysteresis loop (red rectangle in Fig. 11) or calculated from the product of the magnetic flux density B and the magnetic field strength H. The maximum energy density product (BH)$_{max}$ which can be achieved from a magnet of magnetization M is given by

$$(BH)_{max} = \frac{J_r^2}{4\mu_0}$$

(34)

with a further precondition which has to be fulfilled

$$\mu_0 H_c > \frac{J_r}{2} \quad .$$

(35)

However, the maximum energy density product is only available for a rectangular hysteresis loop, which means that the coercivity H_c and the remanent polarization J_r should be large enough, as shown in Fig. 11.
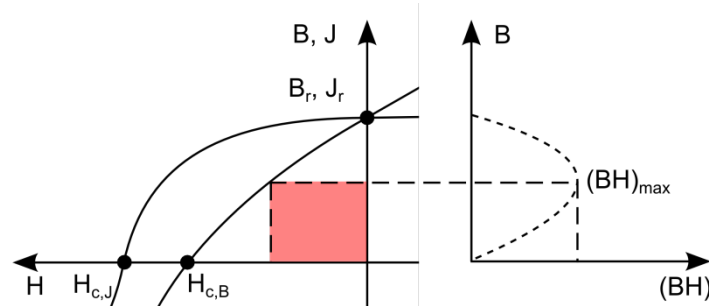
Fig. 11: Illustration of the demagnetization curve of B(H) in the second quadrant and as counterpart the energy density product in the first quadrant.

2.8. Magnetic Materials

In the following Table 2 a brief overview of some well-known magnets is given. The thick line separates soft magnets from hard magnets.

Table 2: Fundamental magnetic properties of relevant magnetic materials [3, 19, 20, 24].

Material	T_c (K)	H_c (kA/m)	J_s (T)	K_1 (J/m³)	$(BH)_{max}$ (kJ/m³)
bcc Fe	1044	0.06	2.15	$4.8 \cdot 10^4$	
hcp Co	1388	4	1.79	$4.5 \cdot 10^5$	
Alnico 5	1210	50	1.41	$6.8 \cdot 10^5$	40
$BaFe_{12}O_{19}$	740	119	0.48	$3.2 \cdot 10^5$	45
FePt	750	159	1.43	$6.6 \cdot 10^6$	406
$SmCo_5$	1020	716	1.22	$17.2 \cdot 10^6$	231
Sm_2Co_{17}	838	800	1.22	$4.2 \cdot 10^6$	294
$Nd_2Fe_{14}B$	588	963	1.61	$4.9 \cdot 10^6$	512

3

Material and Synthesis of (Fe,Co)$_{2-3}$B Alloys

This chapter provides the research base of this thesis. First, under consideration of the literature the phase relations of the binary and the ternary phase diagram and the possible crystal structures of the produced alloys are described in section 3.1. Furthermore, in the sections 3.2 to 3.4 the manufacturing process is presented.

3.1. Phase Relations and Crystal Structures

On the basis of the literature, the binary Fe-B and Co-B phase diagrams and the ternary Fe-Co-B phase diagram have been analysed in detail. The binary phase diagrams shown in Fig. 12 may appear similar because of the electron configuration of Fe and Co differ only in the 3d orbital. Iron (Z =26) and cobalt (Z = 27) are neighbours in the periodic table. By a more detailed examination of these phase diagrams a difference with regard to the phase relations is visible: Both exhibit a 1:1 and a 1:2 phase, but particular attention should be paid to the possible 1:3 phase. It exists in the binary Co-B phase diagram (Fig. 12.a), but in the case of the Fe-B system (Fig. 12.b) the 1:3 phase does not occur.
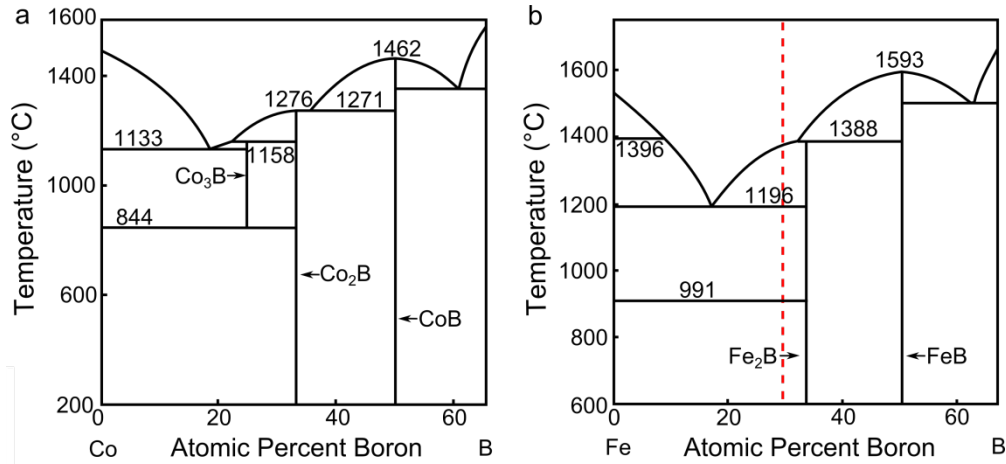

Fig. 12: Binary phase diagram of a) Co-B and b) Fe-B according to [9]. The dashed line determines the exact composition of the (Fe + Co) amount of synthesized (Fe,Co)$_{2-3}$B alloys.

For (Fe,Co)$_{2-3}$B alloys with a relation of Fe/Co < 1, the Co-B system provides a consistent description due to the 1:3 phase. If the ratio is Fe/Co > 1, the Fe-B system is prevailing and a possible (Fe$_{1-x}$Co$_x$)$_3$B structure does not occur. In comparison with the ternary phase

diagram (Fig. 13) a Co reduction below 50 at.% leads to a suppression of the ternary $(Fe_{1-x}Co_x)_3B$ structure. The dashed lines in Fig. 12.b and Fig. 13 correspond to the chosen nominal composition. In the case of the ternary phase relation, the nominal composition lies on the boundary between the (Fe,Co)B and the $(Fe,Co)_2B$ phase.
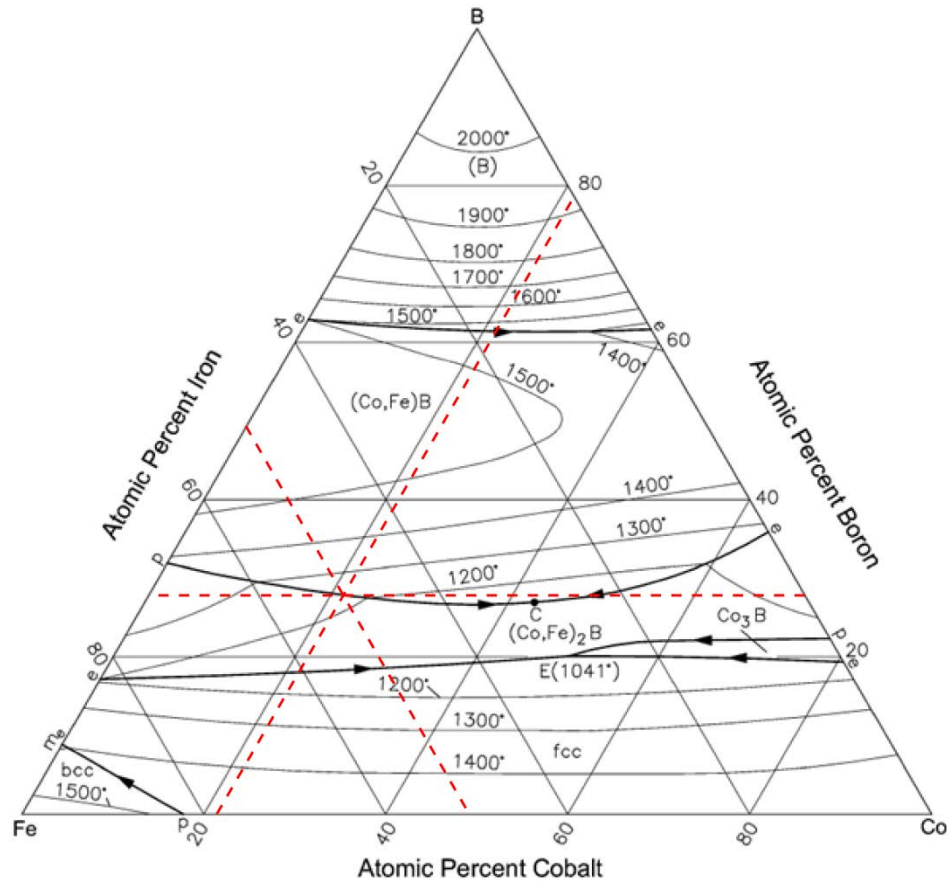

Fig. 13: Ternary phase diagram of B-Co-Fe [25].

A list of all eligible structures for further studies was found in the Pearson's Handbook [26] and is shown in Table 3. The structures marked with an asterisk result from the binary alloys in consideration of the phase diagram using the Vegard's law. These structures were used to identify the diffraction pattern images of the transmission electron microscopy and the X-ray diffraction spectra.

Table 3: Crystal structures in the Fe-B and Co-B systems according to [26].

Structure	a (nm)	b (nm)	c (nm)	System	Space Group	No.	Structure Type
B	0.4910		1.2570	trigonal	R-3m	166	B
Co	0.2506		0.4069	hexagonal	P6$_3$/mmc	194	Mg
Fe	0.2867			cubic	Im-3m	229	W
(Fe,Co)B	0.5392	0.2983	0.4006	orthorhombic	Pnma	62	BFe
Co$_2$B	0.5012		0.4221	tetragonal	I4/mcm	140	Al$_2$Cu
Fe$_2$B	0.5110		0.4249	tetragonal	I4/mcm	140	Al$_2$Cu
(Fe$_{0.7}$Co$_{0.3}$)$_2$B *	0.5082		0.4241	tetragonal	I4/mcm	140	Al$_2$Cu
Co$_3$B	0.5223	0.6629	0.4408	orthorhombic	Pnma	62	Fe$_3$C
Fe$_3$B	0.5428	0.6699	0.4439	orthorhombic	Pnma	62	Fe$_3$C
(Fe$_{0.7}$Co$_{0.3}$)$_3$B *	0.5367	0.6678	0.4430	orthorhombic	Pnma	62	Fe$_3$C

* According to Vegard's law

3.2. Induction Melting

The difficulties linked to the implementation of boron in the compositions were resolved by means of the master alloys Fe$_{80}$B$_{20}$ and Co$_{85}$B$_{15}$ [9]. Both master alloys were manufactured by London & Scandinavian Metallurgical Co. Limited. The desired (Fe$_{1-x}$Co$_x$)$_{71}$B$_{29}$ phase was achieved by adding iron chips (99.95%) and cobalt pieces (99.99%), which were manufactured by Strem Chemicals, Inc.

Table 4: The composition of the master alloys Fe$_{80}$B$_{20}$ and Co$_{85}$B$_{15}$.

Master Alloys			
Fe$_{80}$B$_{20}$		Co$_{85}$B$_{15}$	
Elements	At. %	Elements	At. %
Fe	79.94	Co	84.94
B	19.50	B	14.50
C	0.5	C	0.5
Al	0.03	Al	0.03
Si	0.03	Si	0.03

For the weighing the following equations concerning a desired compound (A$_{1-x}$B$_x$)$_u$C$_v$

$$m_A = \frac{u \cdot (1-x) \cdot M_A \cdot G}{M} \qquad m_B = \frac{u \cdot x \cdot M_B \cdot G}{M} \qquad m_C = \frac{v \cdot M_C \cdot G}{M} \qquad (36)$$

and

$$M = u \cdot (1 - x) \cdot M_A + u \cdot x \cdot M_B + v \cdot M_C \qquad (37)$$

should be considered, where m_A, m_B, m_C are the weighed portions, u, v and x are the atomic percents, M_A, M_B and M_C are the molecular weights and G is the set value of the weight of the material composition of approximately 4.5 g.

The weighing parameters were chosen in a way that a cast ingot of 4.5 g was achieved. For the implementation a scale (Sartorius CP2250-OCE) was utilized. It should be noted that all measurements were carried out with this scale to minimize the uncertainty according to the specific inaccuracy.

For the $(Fe_{0.7}Co_{0.3})_{71}B_{29}$ compound, which is similar to $Fe_{50}Co_{21}B_{29}$, the parameters of the weighing operation are shown in Table 5. The weight of the master alloy for this composition is 1.6243 g.

Table 5: Parameters of the weighing operation for $(Fe_{0.7}Co_{0.3})_{71}B_{29}$.

Element	At.% theory.	Wt.% theory.	Set Value (g)	Actual Value (g)
B	29.0	7.2	0.3248	0.3249
Co	21.3	28.9	1.3003	1.3006
Fe	49.7	63.9	2.8749	2.8757

In order to achieve a compound with the desired composition, the set value was calculated with regard to the atomic percentage. The actual value of the elements reflects the real, weighed quantities and exhibits minimal differences, which lies within the tolerance range. However, the samples were weighted before and after the induction melting. The cast ingot was 0.00981 g lighter after induction melting, but this difference in weight is too small to influence the values of the atomic and weight percent.

After the weighing operations the sample was melted. The common technologies, which are available for selection, are melting in a resistance furnace with the aid of a gas torch, arc melting and inductive or capacity methods. The only precondition for inductive melting is that the material has to be conductive by applying a high frequency field (HF-field) at a coil, eddy currents are generated in the material and as a result the magnetization work is achieved. The material is not homogeneous, therefore the current density of the HF-field is decreasing against the inward of the material. This decrease is frequency-dependent and is described by the skin effect

$$\delta = \frac{1}{2\pi} \sqrt{\frac{\rho \cdot 10^7}{\mu \cdot f}} \quad , \tag{38}$$

where δ is the skin depth, f is the frequency and ρ is the resistivity of the conductor. Another cause for the heat production in the material is the hysteresis loss of the

ferromagnetic solids. The hysteresis can be described as heat which is caused by molecular abrasion. Molecules are known as small magnets which are oriented towards the external field. Their axes follow the reversion of the external field and this goes with the periodicity of the HF-field. As a consequence of this movement the heat arises out of the internal abrasion between the molecules. Before starting the melting process the tube was filled with argon gas again. [27]
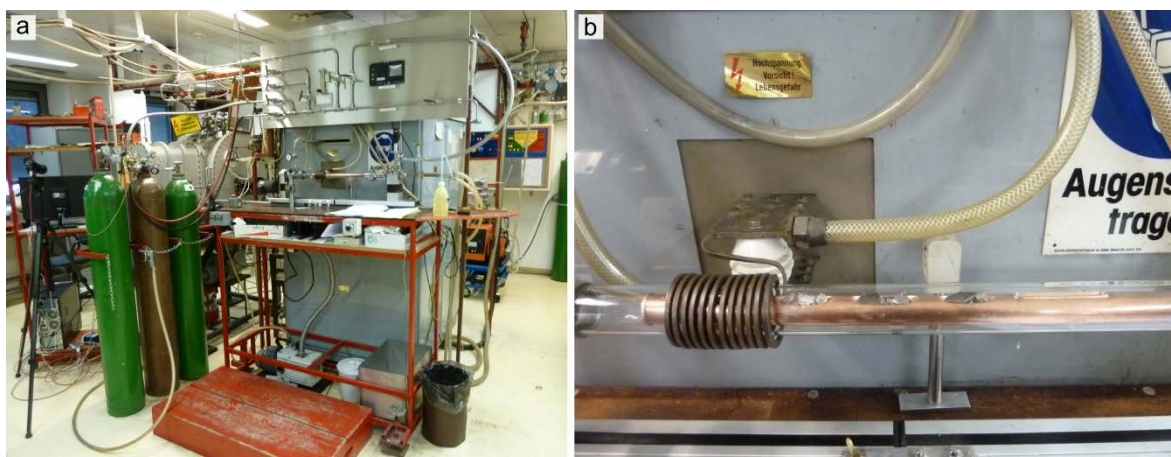

Fig. 14: a) Operating system of the Institute of Solid State Physics, TU Vienna.
b) The samples placed in the slots of the cold boat in the closed system.

The operating system (Fig. 14.a) consists of a RF-generator, Hüttinger Elektronik GmbH 4G 30/400, 78 Freiburg/Br, with an external heat coil (inductor), a cold boat (water-cooled trench) and a gas tank. In general, the material is placed in one of the slots of the cold boat and a quartz tube is given over the cold boat with the material. The unit is a closed system (Fig. 14.b) and the slot with the material has to be placed in directly under the coil.

Table 6: Cast ingots, which were synthesized by induction melting.

Alloy	Composition	Element	At.%	Wt.%	Mass (g)	Master alloy
A	$Co_{71}B_{29}$	B	29.0	7.0	0.32	$Co_{85}B_{15}$
		Co	71.0	93.0	4.18	
		Fe	0.0	0.0	0.00	
B	$Fe_{71}B_{29}$	B	29.0	7.3	0.33	$Fe_{80}B_{20}$
		Co	0.0	0.0	0.00	
		Fe	71.0	92.7	4.17	
C	$(Fe_{0.7}Co_{0.3})_{71}B_{29}$	B	29.0	7.2	0.32	$Fe_{80}B_{20}$
		Co	21.3	28.9	1.30	
		Fe	49.7	63.9	2.88	
D	$(Fe_{0.8}Co_{0.2})_{71}B_{29}$	B	29.0	7.3	0.33	$Fe_{80}B_{20}$
		Co	14.2	19.4	0.87	
		Fe	56.8	73.4	3.30	
E	$(Fe_{0.9}Co_{0.1})_{71}B_{29}$	B	29.0	7.3	0.33	$Fe_{80}B_{20}$
		Co	7.1	9.7	0.44	
		Fe	63.9	83.0	3.73	

This closed system is filled with argon gas 5.0 and afterwards it is evacuated. After 2 or 3 repetitions the process of induction melting is finished. The synthesized cast ingots have a length of 2 cm and a wide of 1 cm. The exact compositions and the utilized master alloys are listed in Table 6 in detail. To get an impression of the cast material structure, the cast ingot of the C alloy was investigated by an analytical high-resolution field emission gun scanning electron microscope (FEI Quanta 200 FEGSEM). An overview of the structure is given in Fig. 15 and exhibits the inhomogeneity of the cast ingot.
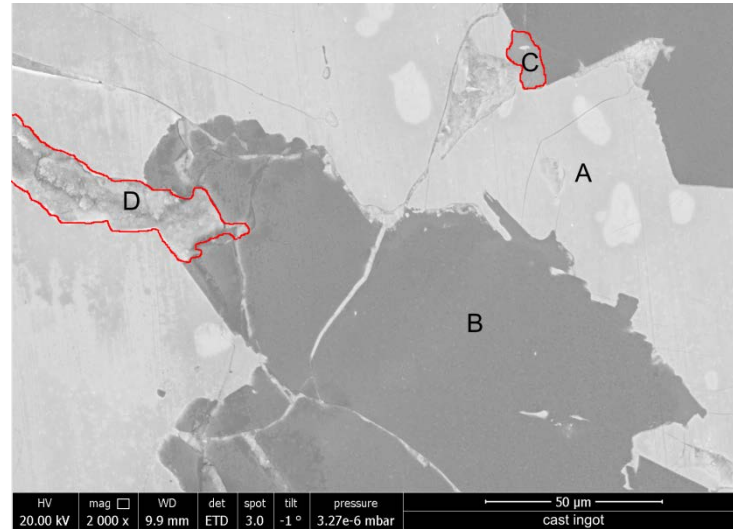
Fig. 15: The SEM image of the C alloy exhibits the inhomogeneous blending of a cast ingot.

Several phases were detected as shown in Fig. 15. The different colour mapping has been determined on the basis of the elements. The EDX analysis of the cast ingots provides an interesting view on the composition, because the most frequent phase A consists mainly of iron with an impurity of carbon. Another phase, which was also very often found, is the area marked with B. This phase consists not only of iron, it also has small impurities, e. g. Al, C, Si, Cu and Mn. In phase C boron was detected for the first time and it was proven with a great percentage. Besides boron there were also iron, cobalt, calcium, carbon and oxygen in a small percentage in this phase. In the last phase D a 2:1 concentration of Fe and Co was measured with impurities of C, O and Si.

3.3. Melt Spinning

In the beginning of the 20th century a process was patented by Strange and Pim, which is now known as melt spinning [28]. These days melt-spun ribbons are interesting for various commercial applications due to their magnetic, anticorrosive and mechanical properties [29]. One big advantage of melt spinning is that the cast material gets heated up to a high temperature and if the desired temperature is reached, the molten cast material gets rapidly

cooled by a copper wheel, which is equal to shock-freezing. The dimensions and the stability of the ribbons are influenced by the pressure, the temperature and the velocity of the Cu-wheel. The velocity of the Cu-wheel determines, whether the ribbon is ductile or brittle [30-32]. In general, the higher the wheel speed, the thinner and more brittle the ribbons are.

Iron and cobalt based alloys are ferromagnetic at room temperature and obtain low coercive fields compared to permanent magnets. These low coercivities are the result of a high homogeneous structure, which does not include vacancies or dislocations. With the right choice of the production parameters high values of the saturation polarization and the coercive field can be achieved. Furthermore, this possibility and the low production costs make melt spinning appear as promising alternative on the way to rare earth free permanent magnets [33].

The melt spinning facility of the Vienna University of Technology was used for the production of the melt-spun ribbons. The facility is situated in a recipient as shown in Fig. 16.a. The recipient consists of stainless steel (X 10 CrNiTi 18, 9) and has a typical wall thickness of 25 mm. Furthermore, the capacity of the recipient is 200 litres and a possible end vacuum of 10^{-6} bar can be reached.
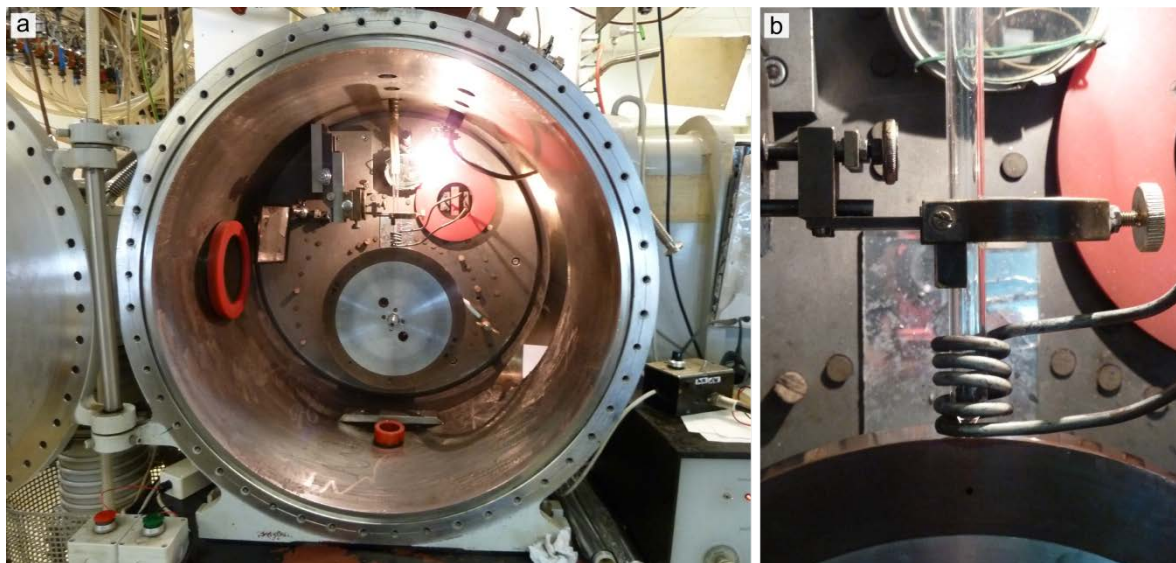
Fig. 16: a) The recipient of the melt spinning facility (Institute of Solid State Physics, TU Vienna) and b) an enlargement of the recipient exhibits the quartz nozzle fixed in a coil.

For the melt spinning, a piece of the cast material is given into the quartz nozzle. This nozzle gets fixed in a coil and connected with a pressure source (helium gas 5.0) as shown in Fig. 16.b. A polished Cu-wheel with a diameter of 30 cm is directly under the nozzle. The experiment works under vacuum or certain atmosphere. During the ribbon casting process the specimen is heated up to 1400 °C with a HF-transformer (200 kHz, 25 kW) and

flows through a quartz nozzle with an opening of 0.3 mm at a pressure difference between the helium gas chamber and the vacuum chamber of 200 mbar. In the next step the molten cast material is cooled by the copper wheel, which is rotating with a velocity of 18.9 m/s, 23.6 m/s, 26.7 m/s, 33 m/s and 37.7 m/s. The molten bath freezes rapidly by a cooling rate of 10^6 K/s and a ribbon is created. The general dimensional properties of this ribbon are: 1 mm for the wide and between 20 - 50 µm for the thickness. [27]

Due to the casting process, the melt-spun ribbon exhibits two surfaces, a matt free surface and a glossy wheel side. The grains closer to the wheel side are smaller in diameter than on the other free wheel side as shown in Fig. 17 [9]. During the scanning electron microscope (SEM) investigation of the ribbons it was determined that with an increasing velocity of the wheel the wide and the thickness become smaller.
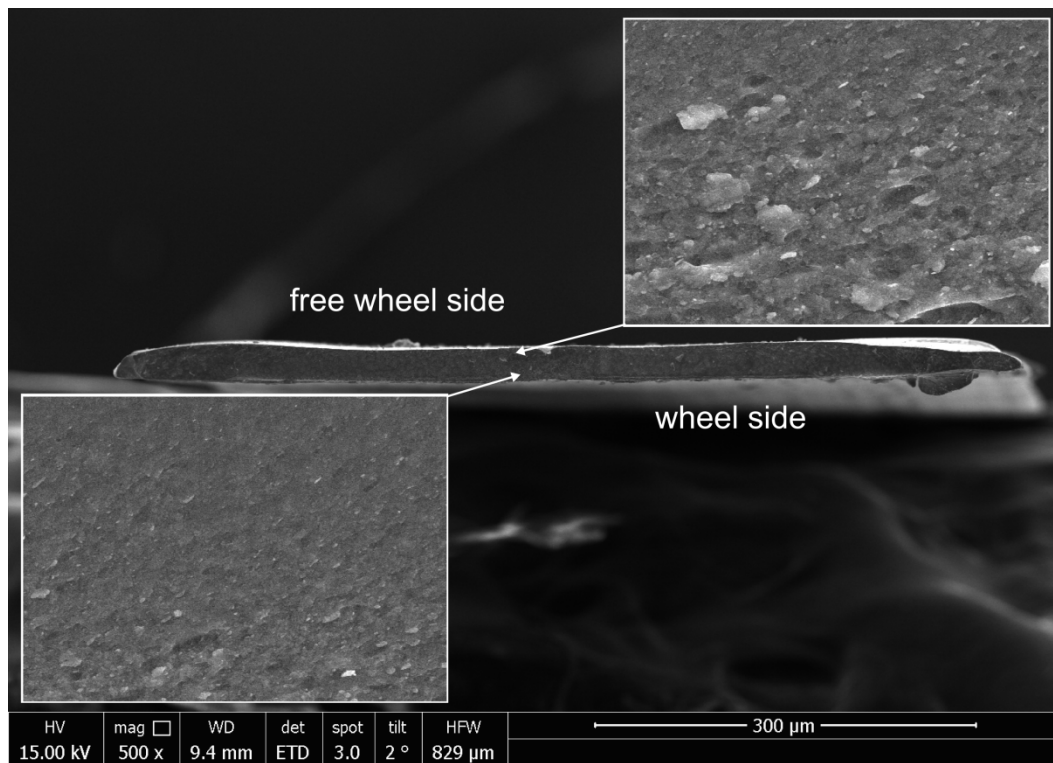
Fig. 17: Cross section of a ribbon with excerpts from the free surface side and the wheel side.

An overview of the cross-section at the centre of the flakes is provided by the SEM image of sample 1700 in Fig. 18. The homogeneity of the microstructure is shown, whereby the grains are randomly orientated. The further investigations of all melt-spun ribbons exhibit that the wide and the thickness of the flakes is decreasing from 840 µm and 35 µm to 630 µm and 21 µm, if the wheel speed is increasing from 18 m/s to 38 m/s.
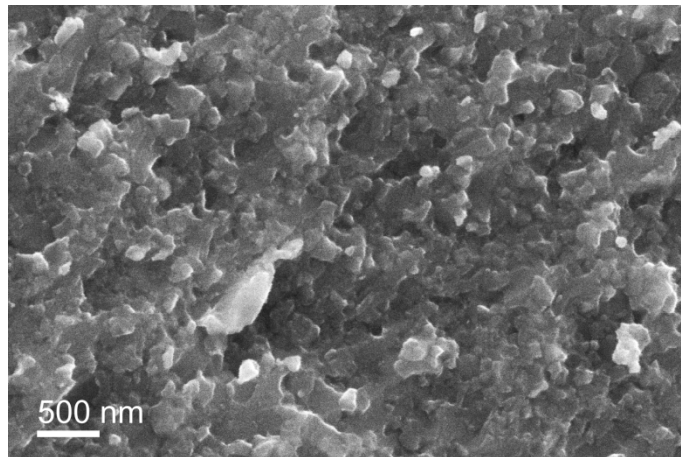
Fig. 18: SEM investigation of sample 1700 shows a homogeneous structure
with randomly orientated grains. The grain size is in the order of 300 nm.

3.4. Annealing

Annealing is a very simple process, which helps to remove stress and homogenize the structure. The sample is heated up, held at certain temperature for a time, and then it is slow cooled. The reasons for annealing are to remove stress and homogenize the structure. The objective of the homogenization is to reduce the different chemical composition. Micro segregation can often be homogenized by annealing. [34]

Based on these knowledge selected melt-spun ribbons were annealed for one hour at 500 °C under vacuum. For the heat treatment a high-temperature chamber furnaces (Naber Typ L47T) was used. The samples were given in small packages, which were prepared with a tantalum foil and these packages were given in a quartz nozzle. The open end of the quartz nozzle was connected with a vacuum pump and the remaining part was given in the furnace for one hour. The tantalum foil was chosen because of its high melting point (around 3269 K), which means that the foil does not react with the sample. In order to prevent an oxidation during the annealing a vacuum pump was connected with the system.

4

Structural and Magnetic Characterization

This chapter presents a brief introduction of the structural and magnetic characterization methods and subsequently the results of the measurements.

4.1. VSM

The vibrating sample magnetometer (VSM) permits the magnetization measurement of the sample in dependence of the external field and different temperatures. The sample is set periodical in vibration with a low frequent oscillating system comparable to a loudspeaker membrane. The device utilizes the induced voltage in a coil system, which is proportional to the magnetic moment of the sample, for a signal extraction. Further probes deliver the applied magnetic field and sample temperature and thereby the hysteresis curve and the temperature can be measured.

The measurements were done at room temperature (298 K) up to a field of 2 T by Quantum Design Physical Property Measurement System (PPMS) - VSM. The starting point of the measurement is at 20 000 Oe and goes to -20 000 Oe with a step size of 50 Oe. Afterwards the external field is gradually increased until 20 000 Oe are reached.
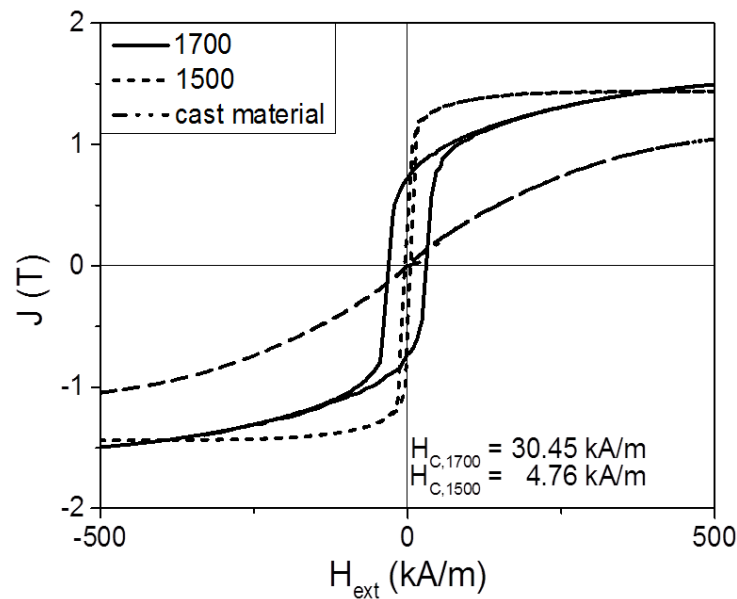
Fig. 19: Hysteresis loops exhibit an increase in the coercive field, while the wheel speed is growing.

The magnetic characterization by PPMS-VSM measurements provides an interesting insight, whether the cast material is optimized by melt spinning or not. The significant difference between the cast material and the melt-spun ribbons, for example sample 1700, is shown in Fig. 19. Based on the VSM-measurements a strong dependence of the coercive field on the wheel velocity with a maximum value at 26.7 m/s. could be observed.

In Table 7 the magnetic properties of the various compounds are listed. One of the results beside the coercivity acquired from the VSM measurements is the magnetic moment (in emu). For the conversion into the polarization (in tesla) the dimensions of the measured flakes were determined by SEM investigations for the calculation of the volume. On the basis of their good magnetic performance, samples 1700 and 1700/6 are outstanding candidates for hard magnetic applications.

Table 7: Magnetic properties of the various compounds.

Sample (rpm)	Alloy	Wheel speed (m/s)	H_C (kA/m)	Magnetic Moment (emu)	Volume (cm³)	J_S (T)
1200	C	18.9	9.21	0.00020	0.00015	1.28
1200 an.	C	18.9	10.70	0.00021	0.00012	1.74
1500	C	23.6	4.76	0.00018	0.00013	1.44
1500 an.	C	23.6	7.57	0.00019	0.00011	1.68
1700	C	26.7	30.45	0.00017	0.00011	1.60
1700/2	B	26.7	5.79	0.00020	0.00015	1.29
1700/3	A	26.7	1.40	0.00019	0.00015	1.20
1700/6	D	26.7	18.50	0.00029	0.00015	1.87
1700/7	E	26.7	5.47	0.00025	0.00015	1.61
1700 an.	C	26.7	22.27	0.00014	0.00010	1.41
2100	C	33.0	18.83	0.00011	0.00012	0.94
2100 an.	C	33.0	9.31	0.00011	0.00010	1.14
2400	C	37.7	12.20	0.00013	0.00007	1.82
2400 an.	C	37.7	9.50	0.00009	0.00006	1.44

Samples marked with an. are annealed

4.2. XRD

X-rays are scattered on crystal lattice because the wave length of X-rays is in the same range as the lattice constant of the crystals. This diffraction effect was discovered by Max von Laue in 1912 and established the modern crystallography. X-ray powder diffraction (XRD) is a rapid technique for qualitative and quantitative phase identification and can provide crystal structure information.

The investigated material is pulverized to orientate as many as possible different planes of this material in diffraction position. Only planes parallel to the specimen surface are measured.

The scattering of X-rays can be treated as reflection on the planes in a crystal lattice. The planes are always parallel and have the same distance d_{hkl}. If the radiation hits one of the planes, single rays get scattered. After the reflection an interference of the scattered single rays results. Constructive and destructive interference depends on the incident angle θ of the radiation, the wave length λ and the plane distance d_{hkl}. For constructive interference and measureable radiation monochromatic radiation has to be used. The phases of the single waves are not allowed to shift at the constructive interference, which means that the path difference has to be a multiple of the wave length λ. [35]

This relation is described by Bragg's Law:

$$n\lambda = 2d_{hkl} \cdot sin\theta \quad . \tag{39}$$

The melt-spun ribbons were grinded to a fine powder by mortar and to minimize extra strain a fluid is added. The powder should have a size of less than approximately 10 µm. Afterwards the powder was placed onto a glass carrier, which was previously applied with a thin layer of vacuum grease. The finished sample is shown in Fig. 20.

Fig. 20: Finished XRD sample on a glass carrier of 5 x 5 cm and the powder
was placed on a 3 x 3 cm area in the middle of the glass carrier.

An overview of the main structures for the XRD measurements is given below. The unit cells were created by the 3D visualization program for structural models VESTA (Visualization for Electronic and STructural Analysis) [36] and the spectra of the powder diffraction were generated by the Java version of the Electron Microscopy image Simulation package written by Stadelmann (JEMS) [37]. The atomic Wyckoff positions of the respective structures are chosen according to the Pearson's Handbook [26]. The exact determination of Fe and Co atoms in the unit cell is uncertain. This difficulty was solved for both atoms by sharing the same position with a specific occupancy.
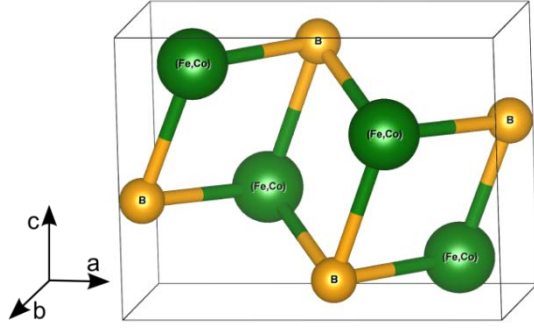
Fig. 21: The unit cell of (Fe,Co)B.

Table 8: Atomic positions of (Fe,Co)B.

Atom	Position	x	y	c	Occ.
B	4c	0.0360	0.2500	0.6100	1.0
Co	4c	0.1800	0.2500	0.1250	0.5
Fe	4c	0.1800	0.2500	0.1250	0.5
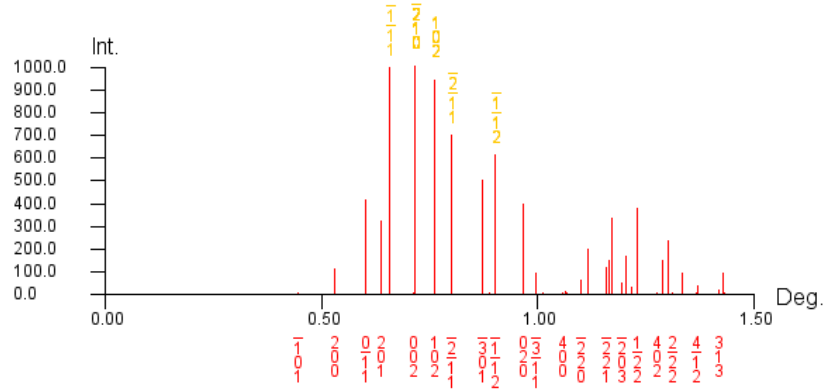
Fig. 22: The (Fe,Co)B spectrum of the powder diffraction
with the five strongest diffraction reflexes.

The (Fe,Co)B structure in Fig. 21 consists of 8 atoms, 4 Fe-Co atoms and 4 B atoms. In this case the occupancy of Fe and Co has 50 percent (Table 8) as prescribed by the literature. The main diffraction reflexes are illustrated in Fig. 22.
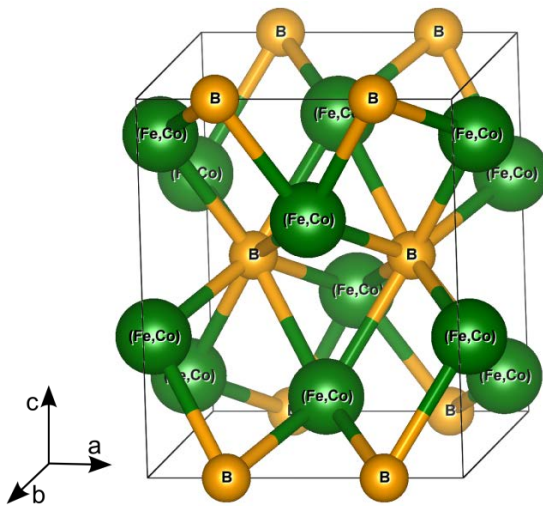
Fig. 23: Unit cell of (Fe,Co)$_2$B.

Table 9: Atomic positions of (Fe,Co)$_2$B.

Atom	Position	x	y	c	Occ.
B	4a	0.0000	0.0000	0.2500	1.0
Co	8h	0.1541	0.6541	0.0000	0.3
Fe	8h	0.1541	0.6541	0.0000	0.7

The unit cell of the $(Fe,Co)_2B$ structure (Fig. 23) has 12 atoms, whereby the outermost boron atoms, which are situated on the top and on the bottom of the unit cell, count only a quarter. Hence, only two boron atoms are resulting. The same applies to the 8 (Fe,Co) atoms, which are placed at the unit cell boundaries on the left and on the right side. The exact atomic positions are listed in Table 9, in which the occupancy of Fe and Co is chosen with respect to the Vegard's law. This choice also concerns the $(Fe,Co)_3B$ structure. The powder diffraction spectrum in Fig. 24 shows the most intense reflexes of this tetragonal structure.
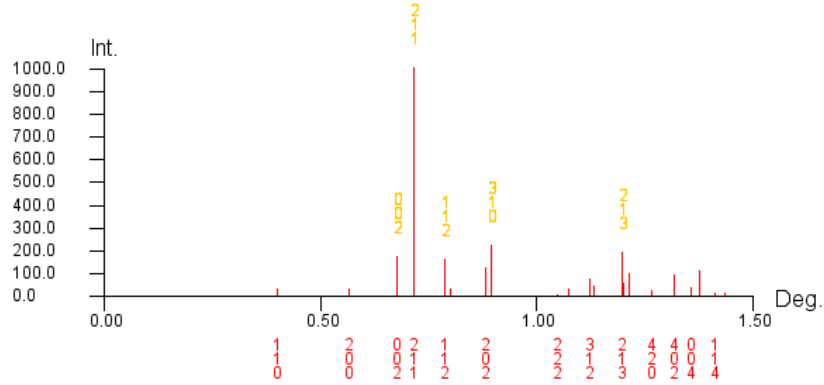
Fig. 24: Powder diffraction spectrum of $(Fe,Co)_2B$ with the five strongest reflexes.

The $(Fe,Co)_3B$ structure in Fig. 25 is an orthorhombic unit cell with 4 B atoms and 12 Fe-Co atoms. The exact atomic positions (Table 10) and the powder diffraction (Fig. 26) of $(Fe,Co)_3B$ are shown in the following.
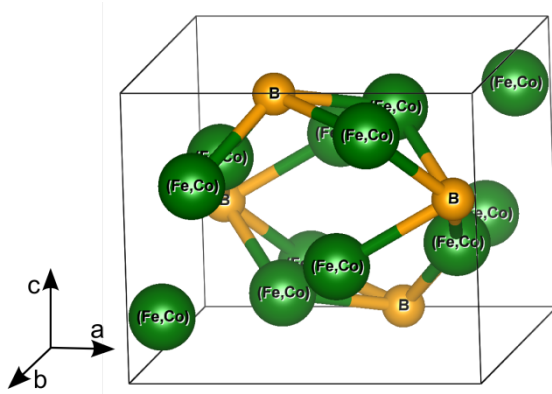
Fig. 25: Unit cell of $(Fe,Co)_3B$.

Table 10: Atomic positions of $(Fe,Co)_3B$.

Atom	Position	x	y	c	Occ.
B	4c	0.8810	0.2500	0.4310	1.0
Co	4c	0.0440	0.2500	0.8370	0.7
Fe	4c	0.0440	0.2500	0.8370	0.3
Co	8d	0.1810	0.0630	0.3370	0.7
Fe	8d	0.1810	0.0630	0.3370	0.3
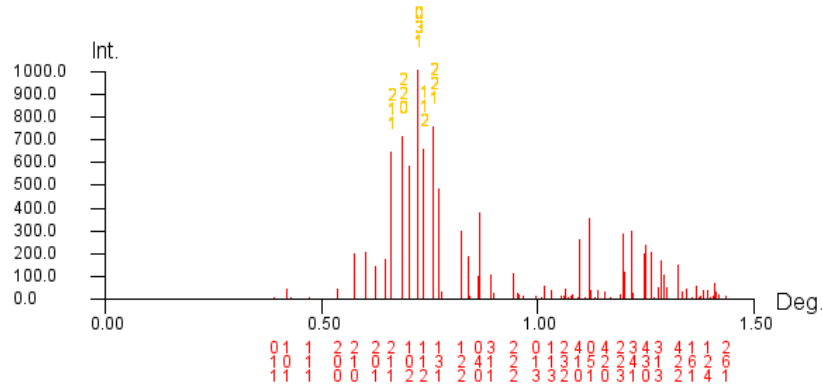
Fig. 26: Powder diffraction spectrum of $(Fe,Co)_3B$ with the five strongest peaks.

The unit cell of the tetragonal Fe_3B structure is shown in Fig. 27 and the unit cell consists of 8 B atoms and 36 Fe atoms. The Fe_3B structure reveals similarities of both main phases $(Fe,Co)_2B$ and $(Fe,Co)_3B$, firstly it has the same crystal system as the 2:1 phase and secondly it has similar lattice parameters as the 3:1 phase.

Fig. 27: Unit cell of Fe_3B-tetragonal.
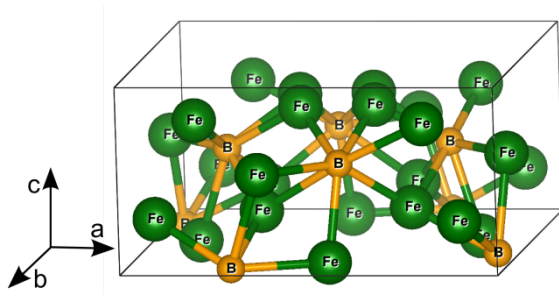
Table 11: Atomic positions of Fe_3B-tetragonal.

Atom	Position	x	y	c	Occ.
B	8g	0.2862	0.0487	0.0193	1.0
Fe	8g	0.0775	0.1117	0.2609	1.0
Fe	8g	0.1351	0.4679	0.0235	1.0
Fe	8g	0.3311	0.2800	0.2476	1.0
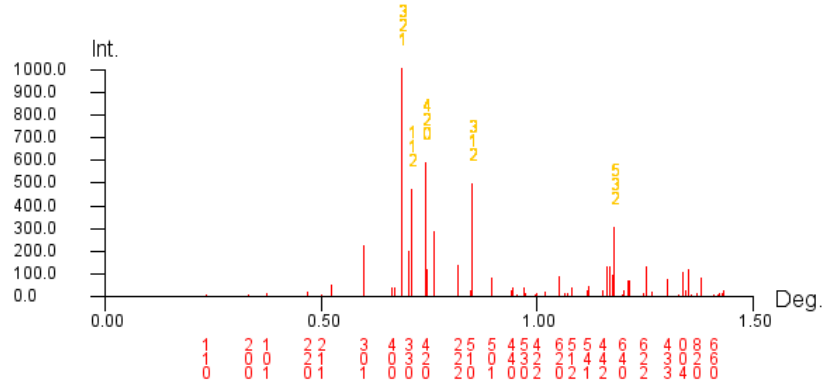
Fig. 28: Powder diffraction spectrum of Fe_3B-tetragonal with the five most intense reflexes.

The characteristic unit cell of the bcc Fe structure is shown in Fig. 29 and the Wyckoff positions are listed in Table 12 as well as the main peaks of the powder diffraction spectrum of Fe in Fig. 30.
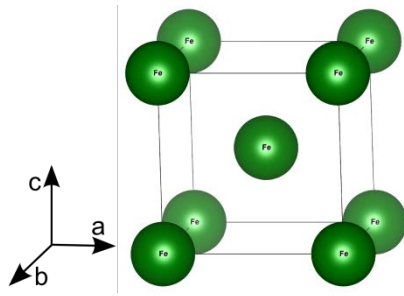
Fig. 29: Unit cell of Fe.

Table 12: Atomic positions of Fe.

Atom	Position	x	y	c	Occ.
Fe	2a	0.0000	0.0000	0.0000	1.0
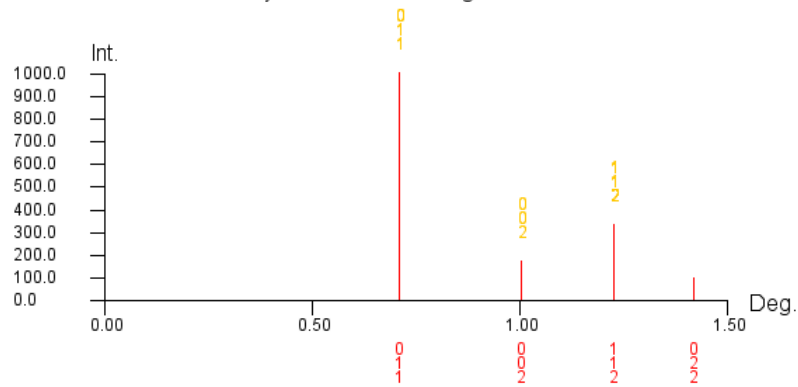
Fig. 30: Powder diffraction spectrum of Fe with the five strongest peaks.

The crystallographic data of the SiO_2 structure as the unit cell, the powder diffraction spectrum and the atomic positions are presented in following Fig. 31-32 and Table 13.
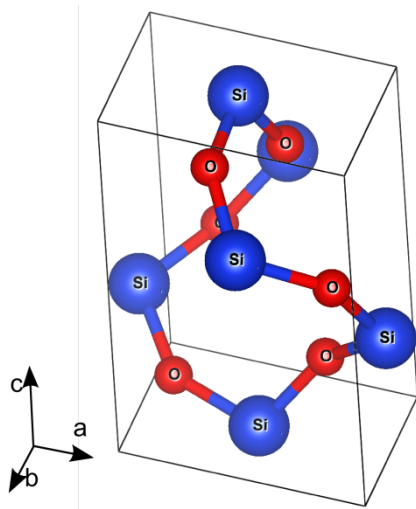
Fig. 31: Unit cell of SiO_2.

Table 13: Atomic positions of SiO_2.

Atom	Position	x	y	c	Occ.
Si	3a	0.4701	0.0000	0.6670	1.0
O	6c	0.4136	0.2676	0.7858	1.0
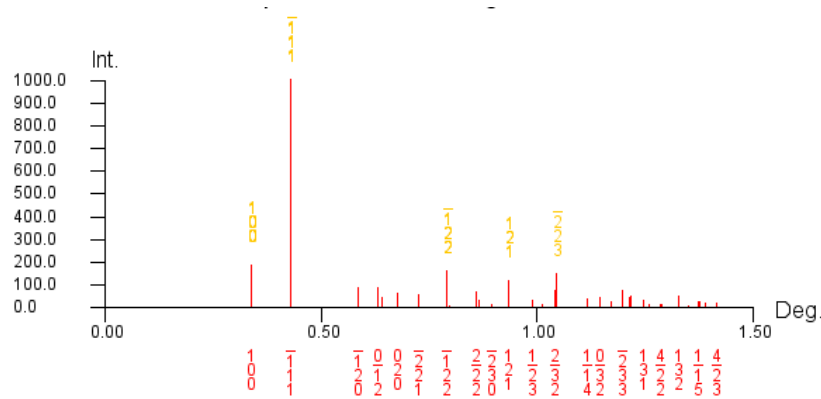
Fig. 32: Powder diffraction spectrum of SiO$_2$ with the five strongest reflexes.

Selected alloys were analysed by the SIEMENS D5000 powder X-ray diffractometer utilizing Cu-Kα radiation. The evaluation of the measurements was conducted by Powder Cell [38] and the results are shown in the following.

In general, almost all samples have a small background compared to their most intense peak. Only sample 1200 with the slowest wheel speed and the highest ductility exhibits a noise background signal (Fig. 33). One reason could be the high ductility of this sample, which made the XRD sample preparation difficult in this case, because more force has to be expend during the grinding. Several phases were detected including (Fe,Co)$_3$B, (Fe,Co)$_2$B and bcc Fe.
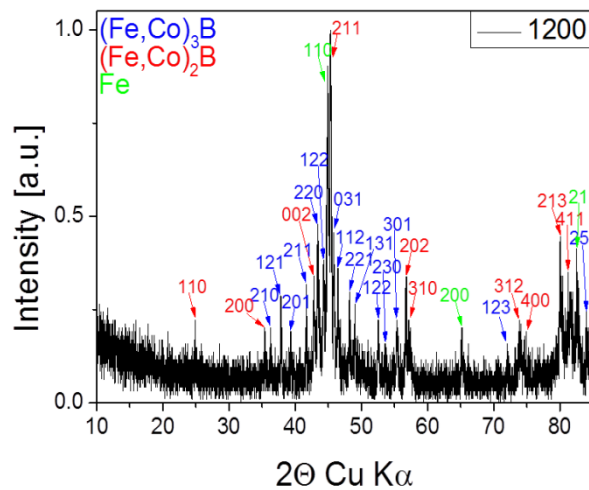
Fig. 33: XRD-spectrum of sample 1200.
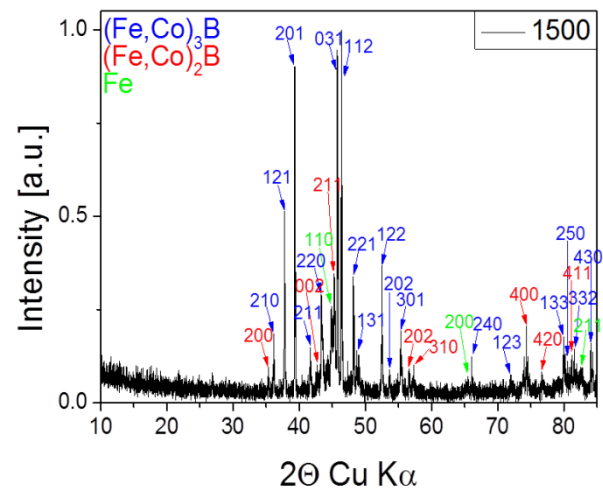
Fig. 34: XRD-spectrum of sample 1500.

The increase of the wheel speed in specimen 1500 decreases the background as shown in Fig. 34. However, the detected phases are still the same as before, whereby the structure of the spectrum has changed and the 3:1 phase became more dominate.

The single phase $(Fe,Co)_2B$ occurs in specimen 1700 and the ratio between background and highest peak is increasing. Due to the significant magnetic properties of sample 1700, the annealed sample 1700 was analysed. During the annealing at over 1 hour Fe and SiO_2 phases have been formed.
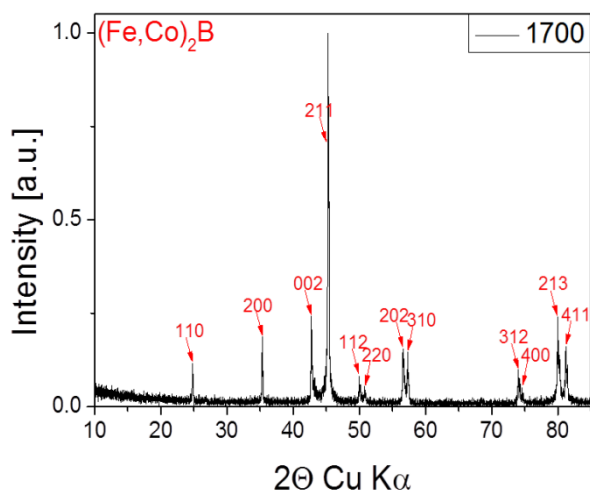
Fig. 35: XRD-spectrum of sample 1700.
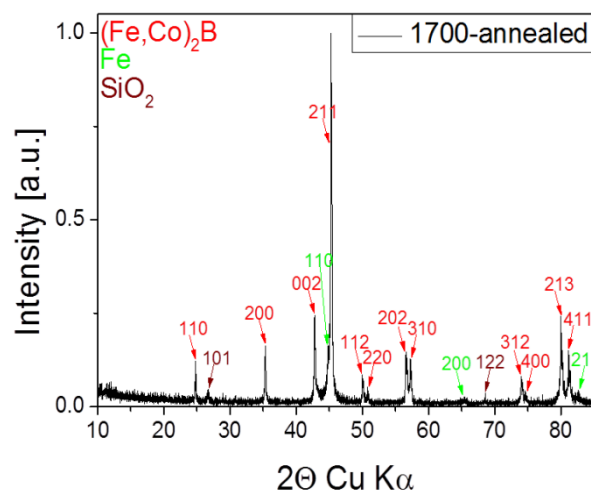
Fig. 36: XRD-Spectrum of sample 1700 an.

The XRD measurement of specimen 2100 exhibits also a single phase of $(Fe,Co)_2B$ with the same characteristics. Nevertheless, a small difference in the intensity of the peaks was detected. The peaks in sample 2100 are smaller compared to the highest peak in this spectrum.
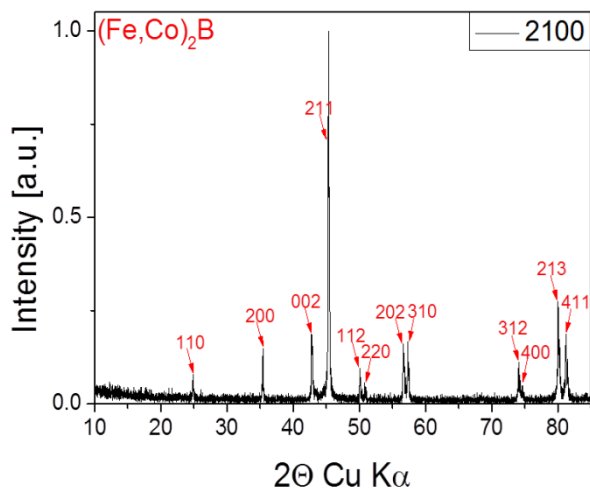
Fig. 37: XRD-spectrum of sample 2100.
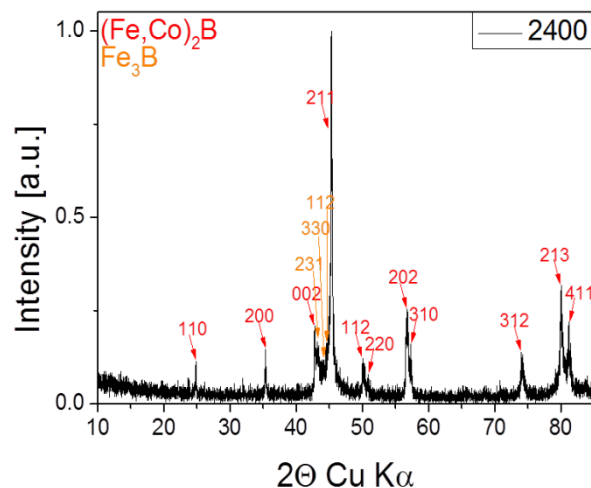
Fig. 38: XRD-spectrum of sample 2400.

As well as the samples 1700 and 2100, the main structure in specimen 2400 is the 2:1 phase. However, the background between (002) and (211) is elevated. This indicates a different phase, which is proven as tetragonal Fe_3B phase.

5

TEM Investigations

This chapter provides an insight of the structure and microstructure of the cast material as well as the melt-spun ribbons.

The ambition of constant improvement drives the humanity forward to new spheres and scientists are traditionally occupied with Goethe's question: "What holds the world together in its inmost folds?". In modern science nanostructures are continuing to grow in importance and the challenge is to enable the investigation and the characterization of these nanostructures.

The light microscope is known since the end of the 16th century and the resolution of a good visible light microscope (VLM) is nowadays in the range of 300 nm [39]. The motivation to get known what is behind the barrier of VLM enabled Knoll and Ruska [40] to invent the transmission electron microscope (TEM) in 1932. In 2009 Erni et al. [41] were able to resolve the atomic structure even of 47 pm in Ge ⟨114⟩ crystal. The TEM operates according to the principal properties of the light microscope, but one huge difference is the utilized probe. The light microscope uses photons and the TEM electrons and the electron differs from the photon by mass and charge, which allows to accelerate the electron to very high energies and due to a small wavelength, a high spatial resolution is provided. The TEM contains the most efficient and versatile tools for determination of morphology, crystallography, lattice defects, chemical analysis, phase transformations, magnetism, optical and electronic properties [39].

The most important imaging possibilities for the characterization of the microstructure in TEM are the bright field (BF) image, the dark field (DF) image and the electron diffraction pattern (DP).

The schematic representation of a TEM is shown in Fig. 39 and describes in the following the beam path from the top to the bottom of the TEM column: The electron source of the TEM is a heated cathode, for example a tungsten tip or in the case of the used microscopes a CeB_6 (FEI TECNAI G20) single crystal or a field emission tip (FEI TECNAI F20). The condenser lenses are focusing the electron beam on the investigated sample. In addition, diffracted beams exist due to the Bragg diffraction besides the primary beam after the

specimen, if the sample is crystalline. The transmitted beams are deflected by the objective lens and the primary beam passing through the objective aperture generates a magnified image at the back focal plane. The intermediate lens and the projector lens enlarge this image and the arising image on the screen is called BF image. In comparison, the DF image results not due to the primary beam, but by a certain Bragg diffraction interference. The diffraction contrast of crystals and defects of the crystal lattice depends on the choice of the Bragg diffraction interference. However, crystal defects as displacements, planar defects and precipitates are identified by means of the BF and the DF image. In the case of an investigation of the crystallography by DP the intermediate lens current has to be changed, the objective aperture removed and a certain selected area diffraction (SAD) aperture used. The whole construction of an electron microscope is situated in the vacuum to ensure that the beam is not deflected by gas atoms. [42, 43]
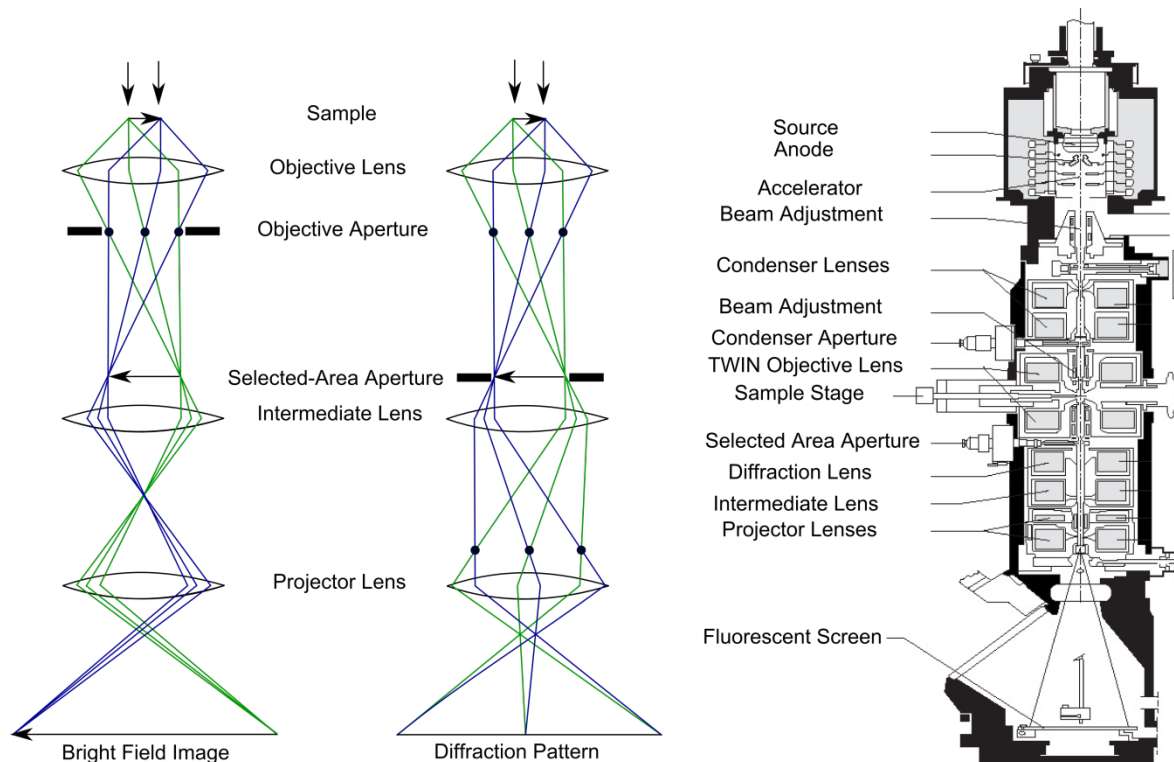
Fig. 39: Scheme of the beam path of a bright field image and a diffraction pattern according to [39] and the construction of a Philips CM 200 TEM according to [44].

Lens aberrations in electron optics play a stronger role than in light optics and reduce the achieved resolution significantly. The crucially lens aberrations are astigmatism, spherical aberration and chromatic aberration. The spherical aberration arises from the field inhomogeneity, which involves that the field configuration does not comply with the criteria of a correct illustration. The chromatic aberrations result from different electron velocities due to different wave lengths, which lead to different refractive powers of the

magnetic lenses. The astigmatism concerns deviations of the rotational symmetry of the lenses caused by small material inhomogeneities, contaminated apertures or magnetic material in the lens field. In general, all lens aberrations are lower with a decrease in the aperture angle α.

A representative overview of the cast material structure is given in Fig. 40. The SEM investigation has shown an inhomogeneity of the structure, which is confirmed by the TEM analysis. Several phases are clearly visible, but nevertheless, some regions of the sample exhibit longitudinal precipitates. Whether they are generated during the production or the sample preparation is uncertain. However, the phase of the precipitates differs from a surrounding phase of the grain.

Fig. 40: Bright field image of the cast material including precipitates with different phase.

The investigation of the alleged different phases revealed that, while it seems to be 2 phases, it is one structure, but different orientations. Figure 41 shows the diffraction analysis of the darker grain and one of its precipitates. In both cases, the found structure related to Table 3 is the 1:1 phase (Fe,Co)B. The bright field image of Fig. 41 exhibits a grain boundary between two grains, whereby one of them has these precipitates. The cast material exhibits large grains in the order of 20 to 100 µm.
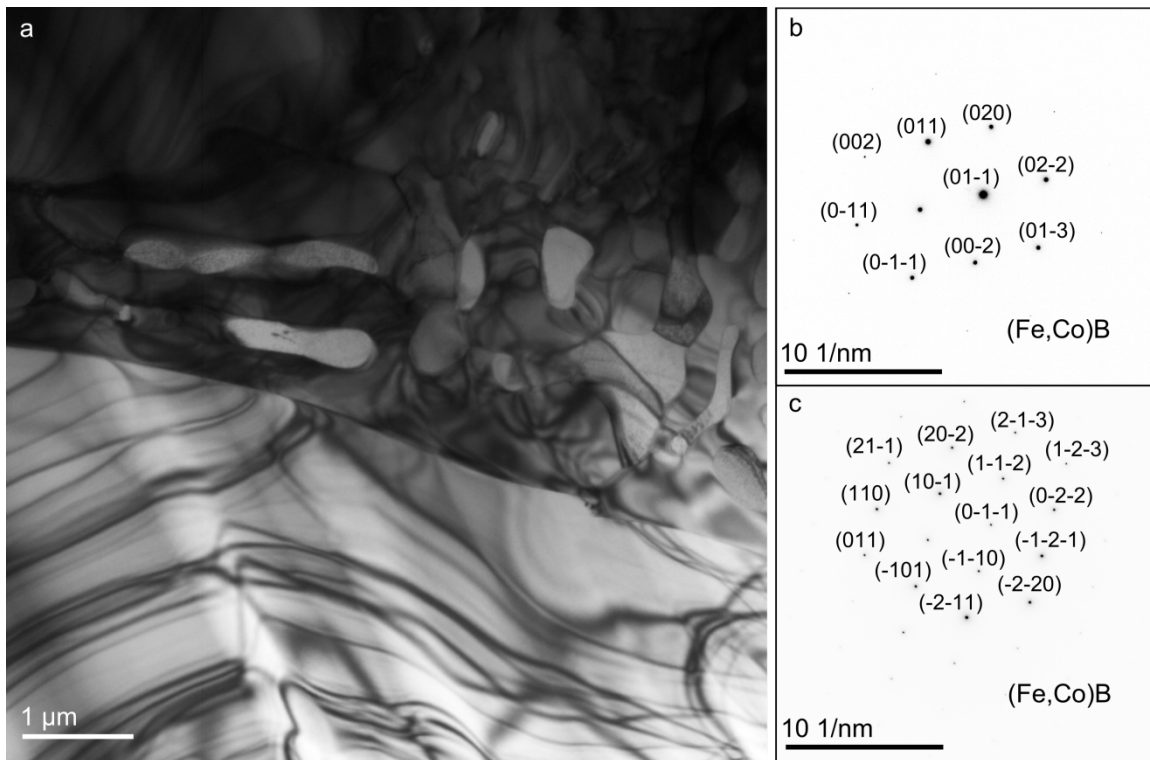
Fig. 41: a) Grain boundary between two grains, whereby the darker grain includes precipitates. b) The diffraction image shows the structure of the precipitates and c) the diffraction pattern is the structure of the dark grain.

The investigation of the melt-spun ribbons is starting with sample 1200 (with a wheel speed of 18.9 m/s), which is characterized by its high ductility compared to the other samples. This effect of a high ductility at a lower wheel speed was confirmed by Barth [30].
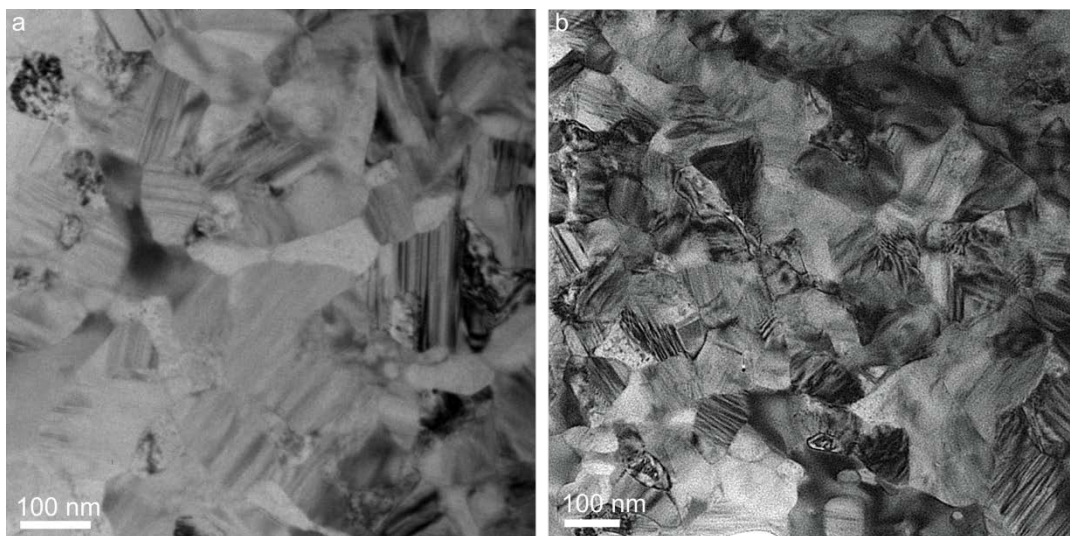
Fig. 42: Two bright field images of sample 1200 and both exhibit tensile stress.

In Fig. 42 both bright field images of sample 1200 show randomly oriented grains and tensile stress. A majority of these grains exhibits heavily fault grains. The size of the grains is in the order of 60 to 150 nm. The analysis of the annealed sample 1200 an. revealed two significant points. On the one hand there is a reduction of the fault grains and on the other one that the grain size increased, as shown in Fig. 43. The grain size increased 2 or 3 times.
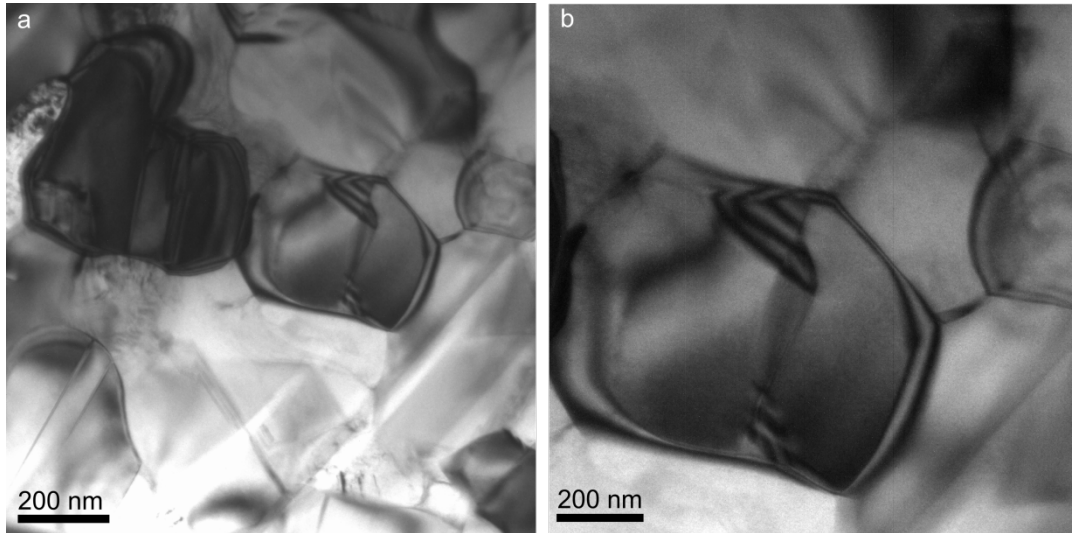
Fig. 43: TEM images of sample 1200 an. at different magnifications.

Specimen 1500 exhibits a high ductility due to its low wheel speed of 23.6 m/s during its production and confirmed the perception of sample 1200. In this case, the TEM image (Fig. 44.a) also shows heavily fault grains. The selected area diffraction image indicates the polycrystalline microstructure of sample 1500 as shown in the small image at the top-right of Fig. 44.a.
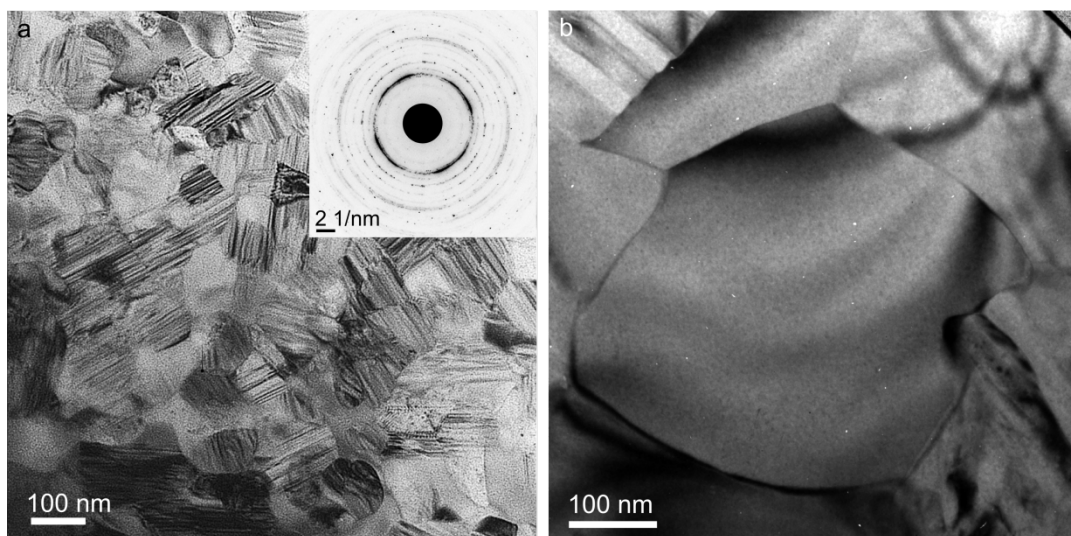
Fig. 44: a) Bright field image of sample 1500 with a polycrystalline selected area diffraction image on the top right side. b) Bright field image of sample 1500 an., which has a grain size of 435 nm.

The size of the grains is in the range of 80 to 150 nm, however, the size increased by annealing about 2 or 3 times as shown in Fig. 44.b. Specimen 1500 an. has less heavily fault grains than specimen 1500, which is in coherence with the samples at a lower wheel speed (1200 and 1200 an.).

The specimen 1700 has the best magnetic performance known from the PPMS measurements and presents a different microstructure compared to the other samples, as shown in Fig. 45. The grain boundaries of this specimen are found to be decorated by precipitates (Fig. 45.c). This behaviour is representative for the microcrystalline microstructure of all inspected specimens at a wheel speed of 26.7 m/s. The phase of the grain marked with region b was identified by evaluation of the selected area diffraction pattern compared to the structures in Table 3 as $(Fe,Co)_2B$.
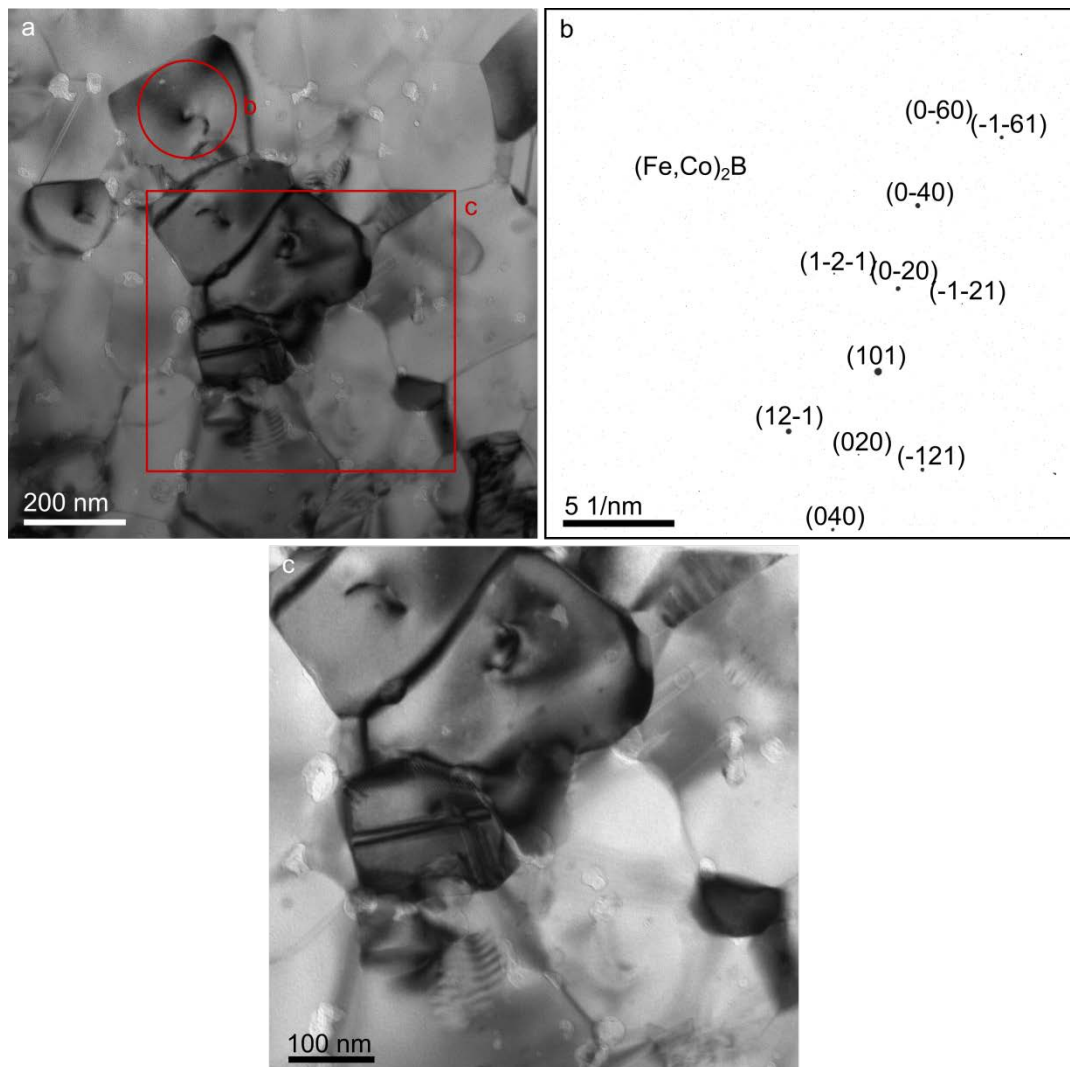
Fig. 45: a) Overview of the microcrystalline microstructure of sample 1700. b) Diffraction pattern of region b in a. c) The grain boundaries are decorated with precipitates.
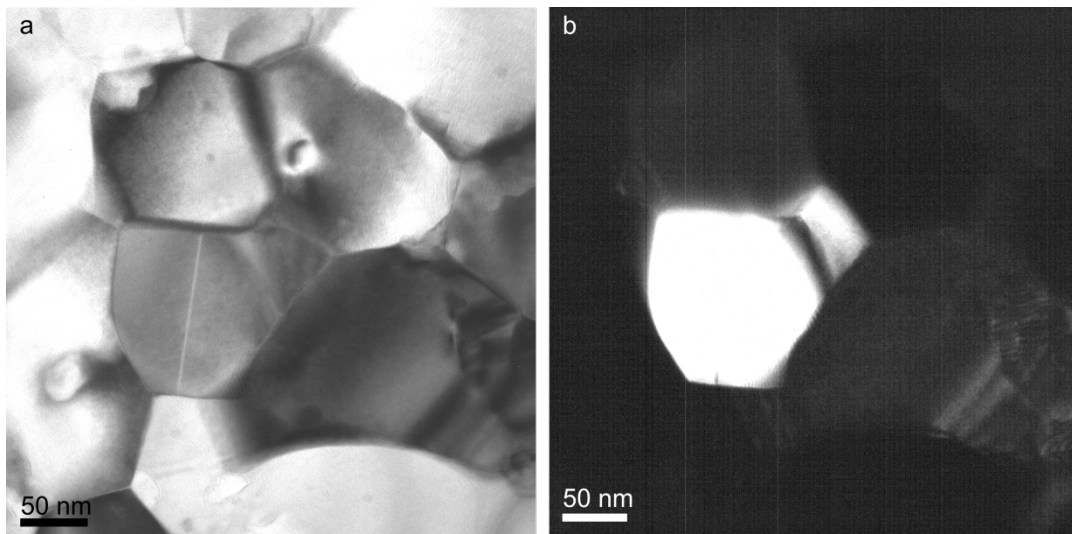
Fig. 46: a) Bright field and b) dark field image of sample 1700.
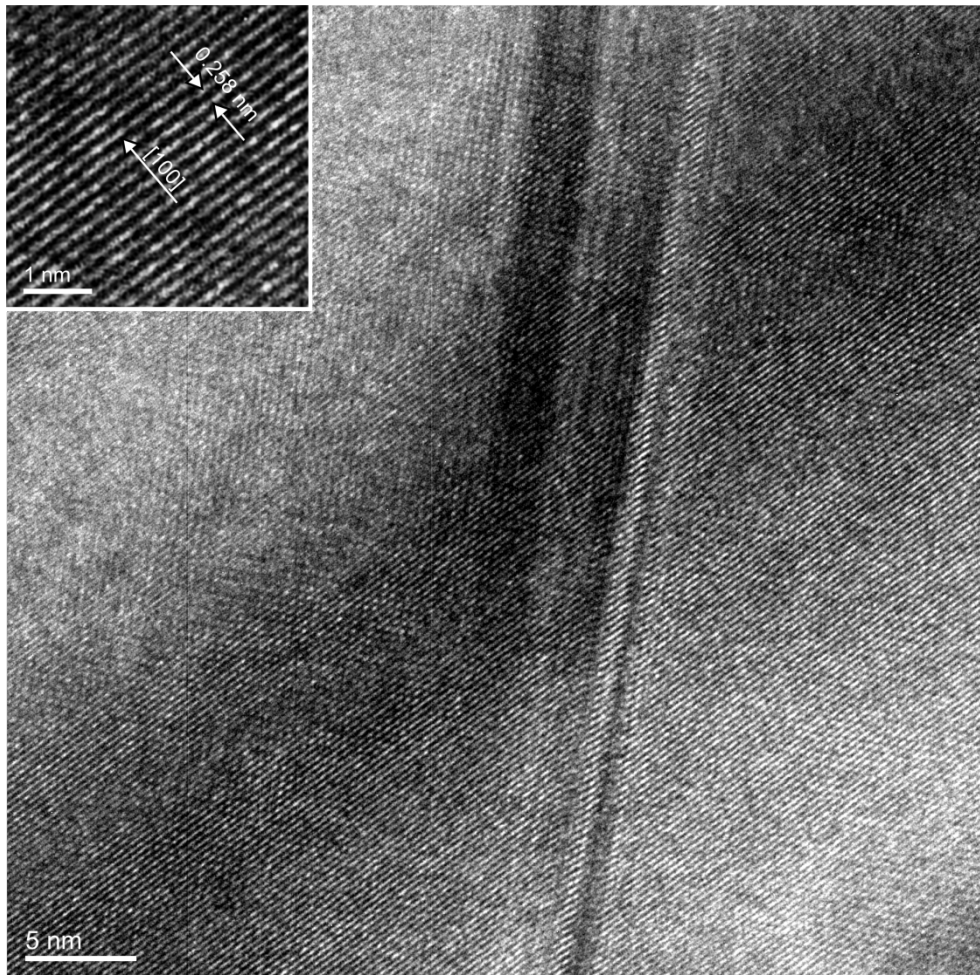
Fig. 47: Planar defects in a grain of sample 1700 with an HR-TEM image at the top left position.

The grains are randomly orientated as shown by comparing the dark field image with the bright field image in Fig. 46 and in addition, a planar defect is illustrated. However, a closer consideration to the planar defect reveals Fig. 47 and the high resolution (HR) image of this area on the top left of this image exhibits the orientation of the grain. In Fig. 48 the bright field image is supplemented by the diffraction rings and exhibits a polycrystalline structure. The grain size is in the order of 300 nm and is consistent with the SEM investigations.
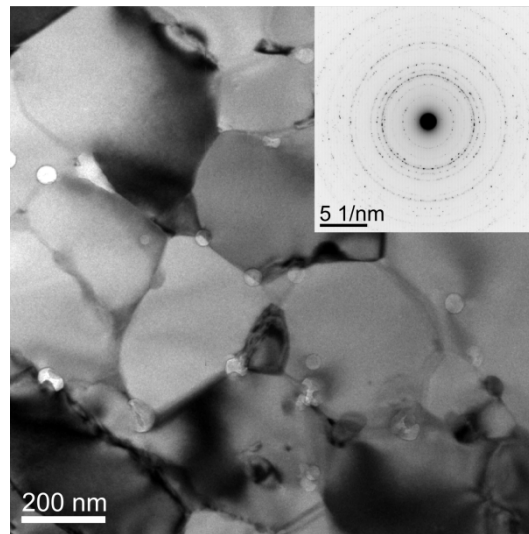
Fig. 48: Bright field image of sample 1700 with a polycrystalline diffraction pattern.

The bright field images of specimen 2100 (Fig. 49), which was produced at a wheel speed of 33 m/s, exhibit a granular microstructure with a grain size of about 100 to 250 nm in diameter.
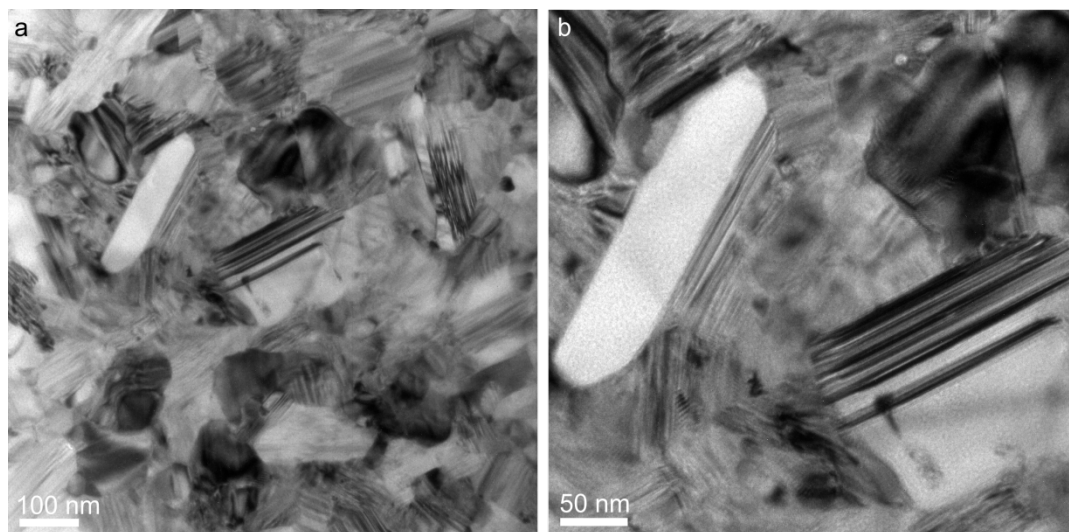
Fig. 49: a) Illustration of a bright field image of sample 2100 at lower magnifications. b) The bright field image of a higher magnification exhibits fault grains and longitudinal grains.

Fig. 49.a shows an overview of the homogeneous distribution of different grains. In Fig. 49.b, heavily faults and longitudinal as well as other grains are shown. However, these defects are not as dominant as in samples with a lower wheel speed (< 26.7 m/s). Sample 2010 exhibits in Fig. 50.a a none orientated microstructure at a different place. In addition, the specimen 2100 an. confirmed the rule by an increase of the grain size between none annealed and annealed, as shown in Fig. 50.b.
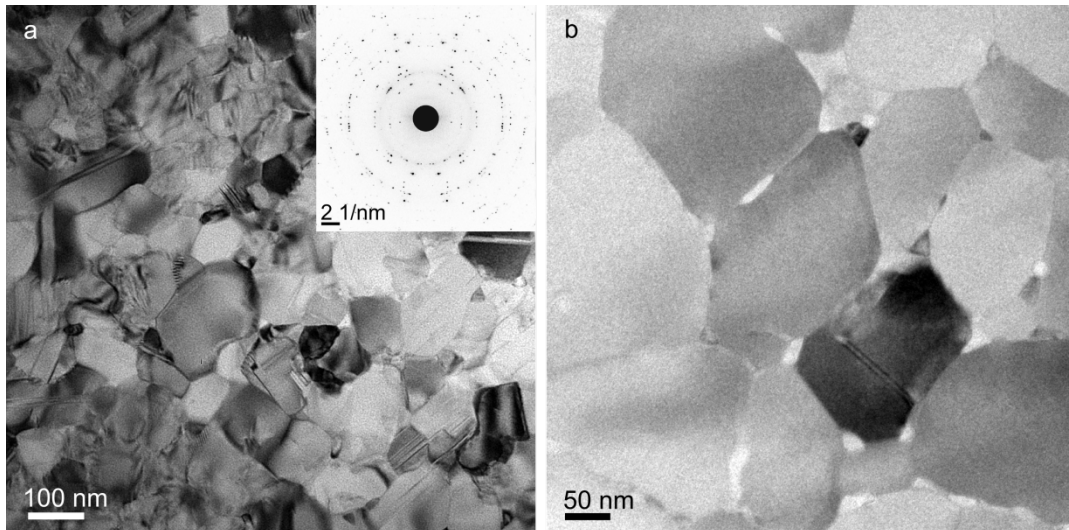

Fig. 50: a) Bright field image of specimen 2100 with a polycrystalline diffraction pattern.
b) The bright field image of sample 2100 an. shows less microcrystalline defects, but precipitates are decorated on the boundaries.

Specimen 2400 shows randomly oriented grains and a polycrystalline pattern in Fig. 51.a.
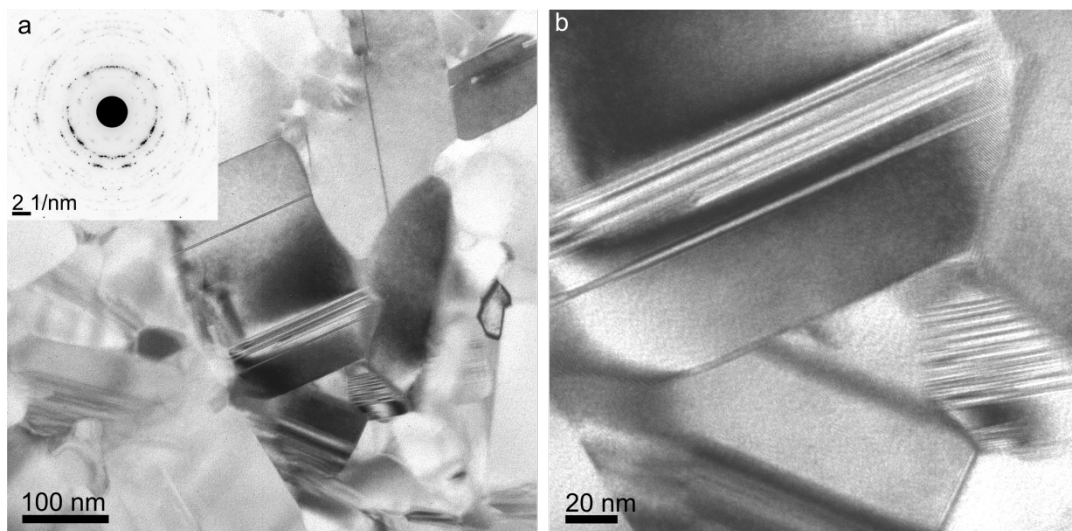
Fig. 51: Bright field images of the microstructure of sample 2400 at two different magnifications exhibit local high planar defects.

The high resolution image of sample 2400 (Fig. 51.b), which was produced at the highest wheel speed of 37.7 m/s, shows local a high planar defect density inside the $(Fe,Co)_2B$ grains. The grain size is in the order of 80 to 250 nm.

5.1. Phase Analysis with Electron Diffraction

In comparison to the XRD results in section 4.2, electron diffraction investigations were done based on a selection of compounds. The compounds are verified by the comparison of the crystal structures of Table 1.
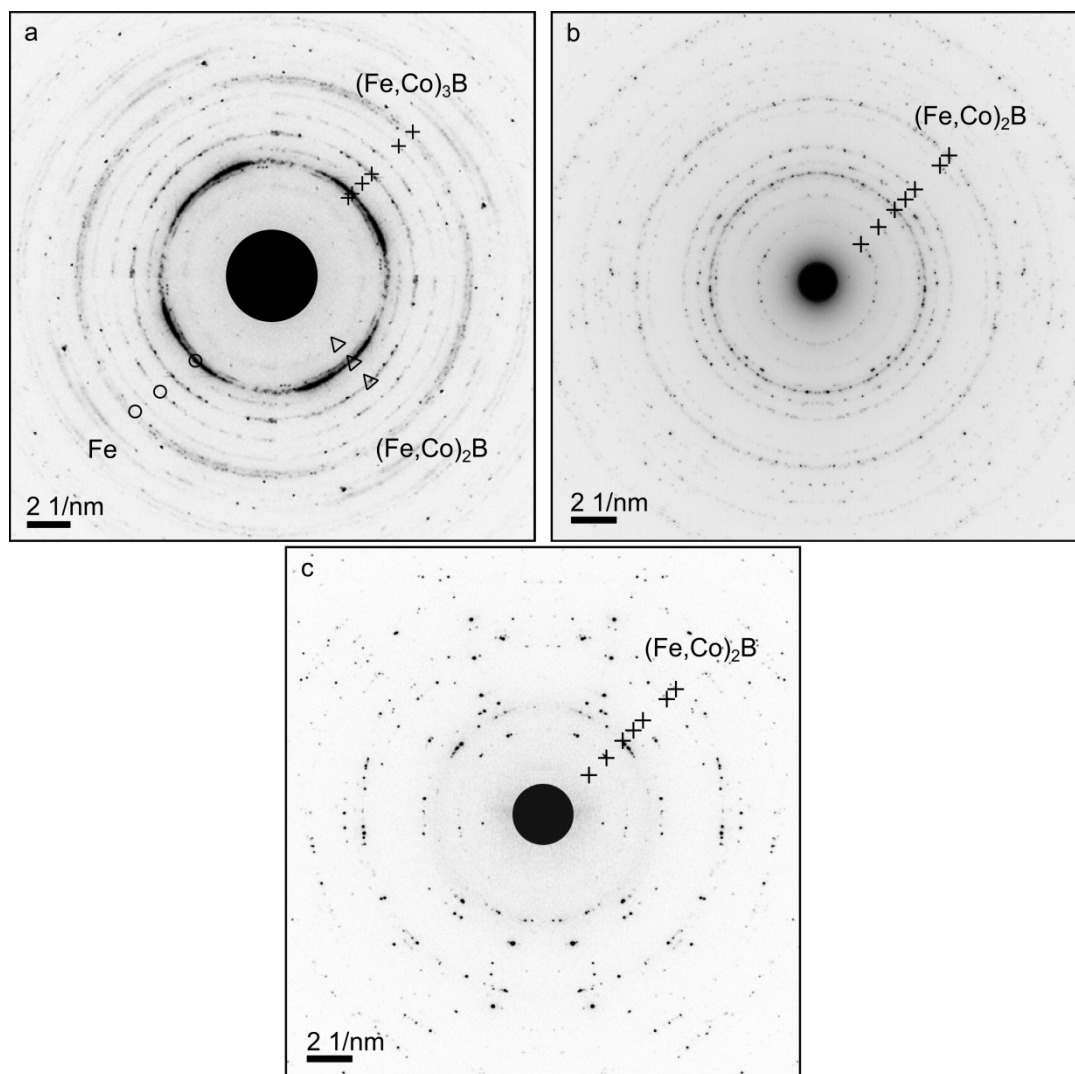

Fig. 52: a) Diffraction rings of sample 1500 with $(Fe,Co)_2B$, $(Fe,Co)_3B$ as well as bcc Fe detected phases. b) Single phase $(Fe,Co)_2B$ was measured for specimen 1700. c) Sample 2100 exhibits a single $(Fe,Co)_2B$ phase.

The selected area diffraction image of specimen 1500 indicates the intergrowth of several phases such as $(Fe,Co)_2B$, $(Fe,Co)_3B$ and bcc Fe as shown in Fig. 52.a. The strongest

diffraction rings of all three structures are very close together. Specimen 1700 was identified by the diffraction patterns of different single phase $(Fe,Co)_2B$ grains (Fig. 52.b). The resulting $(Fe,Co)_2B$ phase of sample 2100 in Fig. 52.c stays in relation to the XRD examinations. These additional investigations of the crystal structure by TEM analysis are in accordance with the XRD measurements in section 4.2.

6

Discussion

This chapter presents the discussion of this thesis and revealed the intermediate steps of the author's decision-making processes during the synthesis and analysis of $(Fe,Co)_{2-3}B$ alloys.

An enhanced research of alternatives to the high performing permanent magnets containing rare earth were supported, apart from the challenge to replace the rare earth elements, an essential reduction is desirable. Since the 1970s the FeCo-B alloys had attracted much attention as Iga [10] reported a significant high magnetocrystalline anisotropy constant of $K_1 = 410$ kJ/m³. The result motivated Takacs et. al. [11] and Coene et. al. [12] to analyse the magnetic properties of the $(Fe,Co)_{2-3}B$ alloys. Over 40 years later, the $(Fe,Co)_{2-3}B$ based alloys are still relevant due to their good magnetic properties as well as economic reasons. These results were the initial impetus in this work and based on the considered compositions in the literature the binary phase diagrams were studied firstly. Iron and Cobalt are both transition metals and exhibit at the first sight an equal phase diagram by means of a similar electron configuration with a slight difference in the 3d orbital. In addition to different values of temperature, there is also a 3:1 phase in the Co-B phase diagram (Fig. 12). The composition of the compounds was chosen with respect to the results of Iga, who is favouring $(Fe,Co)_2B$, and nevertheless it would be interesting to discover a new structure between the 2:1 and the 3:1 phase. The B proportion was determined at 29 at.%, which is in the middle between the two phases, and the FeCo proportion was set at 71 at.%. The distribution of the 71 at.% in the $(Fe_{1-x}Co_x)_{71}B_{29}$ compound depends on the Co concentration x. As known from the literature, the Co concentration should be sufficient small and for the ongoing studies x was set to 0, 0.1, 0.2, 0.3 and 1. The consideration of these concentrations at the ternary phase diagram exhibits the composition of the alloy on the boundary between $(Fe,Co)B$ and $(Fe,Co)_2B$ with a stronger tendency to the 2:1 phase. However, the possibility of a 3:1 phase is excluded. For the induction melting the master alloys $Fe_{80}B_{20}$ and $Co_{85}B_{15}$ were used to avoid all problems relating to the implementation of boron and should grant a homogeneous blending of the weighed components in the cast ingot. However, slight losses had to be accepted, because the master alloys consists of B, Fe or Co and small implementations, as shown in Table 4. These implementations should not influence the microstructure and the

magnetic properties. The compositions of the $(Fe_{1-x}Co_x)_{71}B_{29}$ alloys $(0 \leq x \leq 1)$ were melted in the cold boat with regard to empirical knowledge 3 times and to ensure the homogeneity of the cast material. The investigation of the cast ingot by SEM revealed an inhomogeneity blending of the compositions as shown in Fig. 15. Unfortunately the boron content has separated from iron and several different phases were determined. The impurities of Al, C and Si are not surprising, because their existence is confirmed in the database of the master alloy composition from London & Scandinavian Metallurgical Co. Limited. Oxygen occurred during production and the other elements (Cu, Mn and Ca) are probably related to very small impurities of the master alloy. This assessment is based i. a. from the experiences of other working groups in our institute, who used these master alloys.

The SEM investigation of the melt-spun ribbons showed a homogeneous microstructure with randomly oriented grains (Fig. 18) and compared to the SEM image of the cast material, the melt-casting process was able to intermix the different phases and to reduce the grain size. As expected, the ductility of the samples decreases with increasing wheel speed from 18 m/s to 38 m/s, which is confirmed by [30, 32].
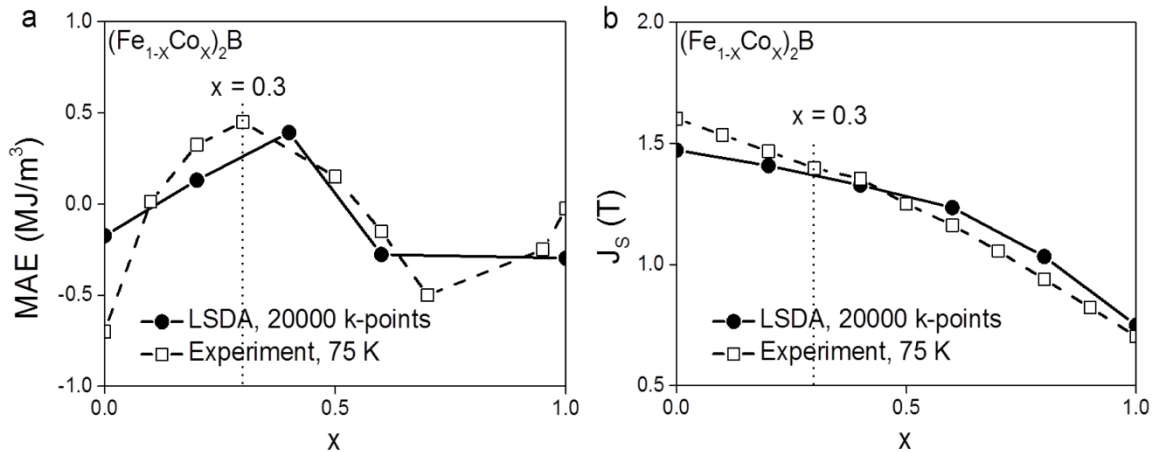
Fig. 53: a) Calculated magnetocrystalline anisotropy energy of $(Fe_{1-x}Co_x)_2B$ as a function of the Co concentration (solid line) in comparison with the measurements (dashed line, [10]). b) The decrease of the magnetization with increasing Co content is shown by the calculated magnetic moments (solid line) and experimental data (dashed line, [16]). The dotted line represents the Co concentration of the $(Fe_{0.7}Co_{0.3})_2B$ [9].

The magnetic measurements by PPMS-VSM present the dependence of the magnetic properties of the alloys on the wheel speed during the melt spinning process as shown in Table 7. A maximum in coercivity of 30 kA/m was achieved by using the C alloy for the melt spinning and at a wheel speed of 26.7 m/s. The change of the cast ingot alloy from C to D enables an increase of the saturation polarization, but with a decrease of the coercivity. In the literature, Wallisch et. al. [9] describes, as shown in Fig. 53.b, a similar behaviour of the saturation polarization to the reduction of the Co concentration x in the

$(Fe_{1-x}Co_x)_2B$ alloy. These results in Fig. 53 are density functional theory (DFT) calculations compared with the experimental data of Iga [10], which exhibit at a Co concentration of x = 0.3 a maximum in the magnetocrystalline anisotropy energy (MAE) with a sufficient high saturation polarization. The magnetic properties of the melt-spun ribbons meet the expectations of these calculations and exceed the values of the saturation polarization in the range of x = 0.2-0.3. The XRD measurement of sample 1700 shows a single $(Fe,Co)_2B$ phase (Fig. 35). In comparison to the other results of the XRD measurements, the single $(Fe,Co)_2B$ phase exists only at certain wheel speeds, 26.7 m/s and 33 m/s, and the reason may be due to an energetic favourable state. For example, the XRD spectrum of specimen 1500 has several phases and at the cooling of the molten bath, which is slower due to the reduced velocity of the wheel speed compared to sample 1700, the cooling rate is not sufficient high to freeze the state, which was reached during the melting and the material has enough time to jump into a new energetically more favourable state. In consideration of the annealed sample 1700, which was annealed for one hour, the structure is changing, although the time for the annealing process is not long. Therefore it is expected that the $(Fe,Co)_2B$ state is not stable. To sum up, melt spinning at a low wheel speed performs in the same way as annealing and is a process to achieve stable states. For certain velocities of the wheel speed, melt spinning enables the shock freezing of instable states, which was achieved for the $(Fe,Co)_2B$ phase in sample 1700 at 26 m/s.

The TEM investigation of the melt-spun ribbons confirmed that sample 1200 is deformed by tensile stress and has heavily fault grains, which is attributed to the slow wheel speed. Sample 1200 an. revealed a reduction of the fault grains as well as an increase of the grain size, which is a characteristic of all annealed samples. In the case of sample 1500, the microstructure has not significantly changed and shows the same tendency. An effect of the structure was detected by specimen 1700. The grains are randomly orientated as before, but the grain boundaries of this sample are decorated by precipitates, which is a characteristic for a wheel speed of 26.7 m/s. The first time of the diffraction pattern determination a single $(Fe,Co)_2B$ phase was detected. At a higher velocity of the wheel speed as in sample 2100, heavily faults beside longitudinal as other grains were discovered. Specimen 2400 exhibits similar results with an increase of high planar defect density. The additional investigations of the crystal structure by TEM are in accordance with the XRD measurements.

Nevertheless, $(Fe,Co)_2B$ alloys have sufficient hard magnetic properties and the theoretical $(BH)_{max}$ is in the range of high performing permanent magnets. By adding these properties to the diagram of Vacuumschmelze according to [1], the $(Fe,Co)_2B$ alloys are

recommendable as a hard magnetic alternative in the gap between the hard ferrites and rare earth magnets [9].
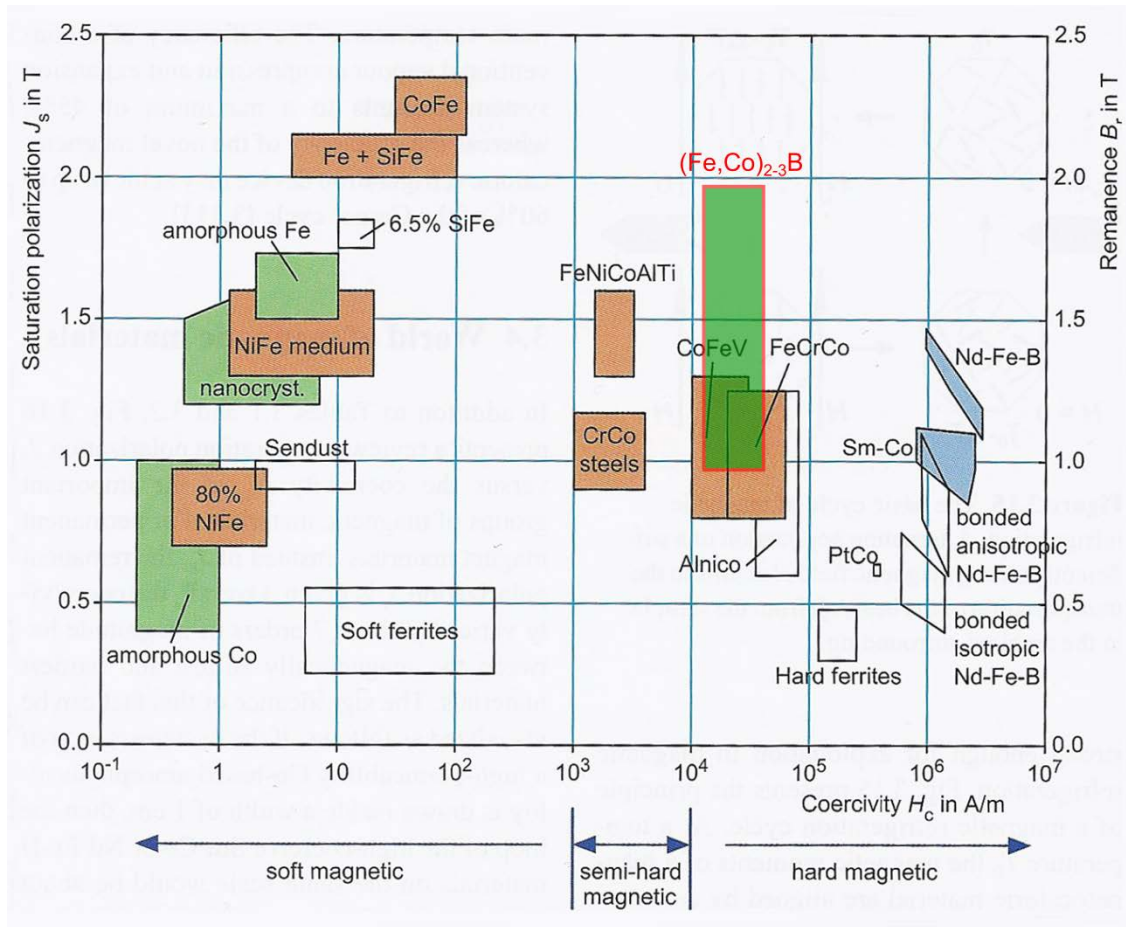

Fig. 54: Review of the important groups of magnetic materials with the implementation of $(Fe,Co)_{2-3}B$ alloys according to Vacuumschmelze [1].

7

Conclusion and Outlook

$(Fe,Co)_{2-3}B$ microcrystalline alloys have been synthesized by melt spinning technique with various wheel speeds in the range of 18 m/s to 38 m/s and under a constant pressure difference between the He gas chamber and the vacuum chamber of 200 mbar. The magnetic properties of the cast material and the ribbons were measured by PPMS-VSM and the crystallography of selected ribbons was analysed by XRD. In addition, the microcrystalline microstructure of the cast material and the ribbons was investigated by nanoanalytical electron microscopy. The highest value of the coercive field $\mu_0 H_c = 30.5$ kA/m was achieved with a wheel speed of 26.7 m/s for the $(Fe_{0.7}Co_{0.3})_{71}B_{29}$ alloy. The material is appropriate for hard magnetic applications due to its high saturation polarisation and high Curie temperature of $T_c = 935$ K as reported by Jian [14]. The remarkable results from the literature [9, 10, 13-16], which possess a high saturation polarisation at a Co concentrations x around 0.3 - 0.4 for $(Fe_{1-x}Co_x)_2B$ alloys have been confirmed by the experimental study on microcrystalline melt-spun ribbons. The theoretical $(BH)_{max}$ of $(Fe,Co)_{2-3}B$ microcrystalline alloys seems to be promising and is in the range of high performing permanent magnets.

Nevertheless, the value of the coercivity, which was achieved by the melt-spinning technique, is not yet sufficient high enough for a permanent magnet application due to its inhomogeneous grain size distribution and its random grain orientation. However, $(Fe_{0.7}Co_{0.3})_{71}B_{29}$ alloys are a potential solution for novel hard magnetic materials in the gap between hard ferrites and rare earth magnets. [9]

On the path towards high performing permanent magnets, $(Fe_{0.7}Co_{0.3})_2B$ alloys provide a good foundation for further studies. One opportunity to improve the magnetic properties of $(Fe_{0.7}Co_{0.3})_2B$ alloys is to add a small amount of rare earth elements or heavy transition metals by substitution of some Fe and/or Co in the concentration as discussed by Edström et. al. [16].

Appendix

A. Remaining Data of the Crystal Structures

hkl-Table of Fe

Table 14: Crystallographic data of Fe.

h	k	l	d^{-1} (nm^{-1})	d (nm)	2 Theta (°)	Intensity	Multiplicity
1	0	0	4.608	0.217	37.99	240	6
0	0	2	4.915	0.203	40.51	265	2
1	0	1	5.222	0.191	43.03	1000	12
1	0	2	6.737	0.148	55.52	151	12
1	1	0	7.981	0.125	65.72	172	6
1	0	3	8.694	0.115	71.62	190	12
2	0	0	9.215	0.109	75.92	25	6
1	1	2	9.373	0.107	77.18	191	12
2	0	1	9.538	0.105	78.55	134	12
0	0	4	9.83	0.102	80.96	26	2

hkl-Table of (Fe,Co)B

Table 15: Crystallographic data of (Fe,Co)B.

h	k	l	d^{-1} (nm^{-1})	d (nm)	2 Theta (°)	Intensity	Multiplicity
1	0	1	3.092	0.323	25.50	0	4
2	0	0	3.684	0.271	30.37	107	2
0	1	1	4.179	0.239	34.43	413	4
2	0	1	4.443	0.225	36.61	315	4
1	1	1	4.567	0.219	37.64	995	8
0	0	2	4.967	0.201	40.91	3	2
2	1	0	4.986	0.201	41.08	1000	4
1	0	2	5.297	0.189	43.66	936	4
2	1	1	5.571	0.18	45.89	695	8
3	0	1	6.058	0.165	49.90	496	4
2	0	2	6.184	0.162	50.94	2	4
1	1	2	6.273	0.159	51.68	612	8
0	2	0	6.722	0.149	55.35	391	2
3	1	1	6.928	0.144	57.07	85	8

h	k	l	d^{-1} (nm^{-1})	d (nm)	2 Theta (°)	Intensity	Multiplicity
2	1	2	7.038	0.142	57.98	0	8
4	0	0	7.367	0.136	60.68	0	2
1	2	1	7.399	0.135	60.96	5	8
3	0	2	7.43	0.135	61.19	2	4
2	2	0	7.665	0.13	63.14	44	4
1	0	3	7.674	0.13	63.20	9	4
4	0	1	7.775	0.129	64.06	195	4
2	2	1	8.057	0.124	66.35	110	8
4	1	0	8.098	0.123	66.69	145	4
3	1	2	8.154	0.123	67.15	278	8
0	1	3	8.173	0.122	67.32	53	4
2	0	3	8.311	0.12	68.47	44	4
0	2	2	8.357	0.12	68.81	1	4
1	1	3	8.378	0.119	68.98	162	8
4	1	1	8.47	0.118	69.79	23	8
1	2	2	8.558	0.117	70.47	371	8
4	0	2	8.885	0.113	73.17	0	4
2	1	3	8.965	0.112	73.85	142	8
3	2	1	9.049	0.111	74.54	227	8
2	2	2	9.133	0.109	75.23	1	8
3	0	3	9.275	0.108	76.38	90	4
4	1	2	9.499	0.105	78.27	0	8
5	0	1	9.538	0.105	78.55	32	4
3	1	3	9.866	0.101	81.25	14	8
0	0	4	9.933	0.101	81.82	84	2
4	2	0	9.973	0.1	82.16	0	4

hkl-Table of (Fe,Co)$_2$B

Table 16: Crystallographic data of (Fe,Co)$_2$B.

h	k	l	d^{-1} (nm^{-1})	d (nm)	2 Theta (°)	Intensity	Multiplicity
1	1	0	2.783	0.359	22.92	27	4
2	0	0	3.936	0.254	32.43	22	4
0	0	2	4.716	0.212	38.85	166	2
2	1	1	4.992	0.2	41.14	1000	16
1	1	2	5.476	0.183	45.09	155	8
2	2	0	5.566	0.18	45.84	27	4
2	0	2	6.143	0.163	50.59	120	8
3	1	0	6.223	0.161	51.28	216	8
2	2	2	7.295	0.137	60.10	0	8
3	2	1	7.477	0.134	61.59	22	16

3	1	2	7.808	0.128	64.29	69	16
4	0	0	7.871	0.127	64.86	36	4
2	1	3	8.331	0.12	68.64	189	16
3	3	0	8.349	0.12	68.75	52	4
4	1	1	8.449	0.118	69.61	92	16
4	2	0	8.8	0.114	72.48	20	8
4	0	2	9.176	0.109	75.57	84	8
0	0	4	9.433	0.106	77.69	32	2
3	3	2	9.589	0.104	78.95	107	8
1	1	4	9.835	0.102	81.02	3	8
4	2	2	9.984	0.1	82.22	3	16

hkl-Table of (Fe,Co)$_3$B

Table 17: Crystallographic data of (Fe,Co)$_3$B.

h	k	l	d^{-1} (nm^{-1})	d (nm)	2 Theta (°)	Intensity	Multiplicity
0	1	1	2.709	0.369	22.35	1	4
1	0	1	2.927	0.342	24.12	35	4
0	2	0	2.995	0.334	24.69	0	2
1	1	1	3.288	0.304	27.10	1	8
2	0	0	3.727	0.268	30.71	38	2
2	1	0	4.016	0.249	33.12	191	4
1	2	1	4.188	0.239	34.49	197	8
2	0	1	4.357	0.23	35.92	140	4
0	0	2	4.515	0.221	37.18	169	2
2	1	1	4.607	0.217	37.99	641	8
2	2	0	4.781	0.209	39.42	707	4
1	0	2	4.884	0.205	40.22	578	4
0	3	1	5.028	0.199	41.42	1000	4
1	1	2	5.109	0.196	42.11	654	8
2	2	1	5.287	0.189	43.54	749	8
1	3	1	5.362	0.187	44.18	476	8
0	2	2	5.418	0.185	44.63	26	4
1	2	2	5.729	0.175	47.21	290	8
2	3	0	5.837	0.171	48.07	180	4
2	0	2	5.854	0.171	48.24	6	4
0	4	0	5.99	0.167	49.33	94	2
3	0	1	6.029	0.166	49.68	258	4
2	1	2	6.043	0.165	49.79	113	8
3	1	1	6.212	0.161	51.17	102	8
2	3	1	6.258	0.16	51.57	18	8

2	2	2	6.576	0.152	54.14	104	8
1	3	2	6.636	0.151	54.66	18	8
1	4	1	6.667	0.15	54.89	14	8
3	2	1	6.732	0.149	55.46	5	8
0	1	3	6.936	0.144	57.12	5	4
1	0	3	7.024	0.142	57.87	2	4
2	4	0	7.055	0.142	58.10	52	4
1	1	3	7.182	0.139	59.19	28	8
3	0	2	7.186	0.139	59.19	0	4
3	1	2	7.34	0.136	60.45	4	8
2	3	2	7.379	0.136	60.79	6	8
2	4	1	7.407	0.135	61.02	38	8
4	0	0	7.454	0.134	61.42	1	2
0	4	2	7.501	0.133	61.76	4	4
3	3	1	7.519	0.133	61.94	11	8
4	1	0	7.603	0.132	62.62	0	4
1	2	3	7.636	0.131	62.91	258	8
1	4	2	7.729	0.129	63.66	1	8
2	0	3	7.73	0.129	63.66	2	4
3	2	2	7.785	0.128	64.11	63	8
4	0	1	7.788	0.128	64.17	285	4
0	5	1	7.82	0.128	64.40	32	4
2	1	3	7.874	0.127	64.86	0	8
4	1	1	7.931	0.126	65.32	32	8
4	2	0	8.033	0.124	66.18	7	4
1	5	1	8.039	0.124	66.23	26	8
0	3	3	8.127	0.123	66.92	0	4
2	2	3	8.29	0.121	68.30	10	8
1	3	3	8.338	0.12	68.70	266	8
4	2	1	8.344	0.12	68.75	12	8
2	5	0	8.364	0.12	68.87	100	4
2	4	2	8.376	0.119	68.98	11	8
3	3	2	8.474	0.118	69.79	295	8
3	4	1	8.499	0.118	70.02	16	8
2	5	1	8.663	0.115	71.33	192	8
4	3	0	8.703	0.115	71.68	227	4
4	0	2	8.714	0.115	71.79	2	4
3	0	3	8.782	0.114	72.31	198	4
4	1	2	8.842	0.113	72.82	0	8
3	1	3	8.908	0.112	73.40	45	8
1	5	2	8.94	0.112	73.63	161	8

2	3	3	8.941	0.112	73.63	0	8
0	6	0	8.985	0.111	74.03	101	2
4	3	1	8.991	0.111	74.03	3	8
0	0	4	9.03	0.111	74.37	43	2
4	2	2	9.215	0.109	75.92	11	8
1	0	4	9.22	0.108	75.92	89	4
1	4	3	9.231	0.108	76.03	52	8
3	2	3	9.278	0.108	76.43	25	8
1	1	4	9.341	0.107	76.95	37	8
3	4	2	9.355	0.107	77.06	13	8
1	6	1	9.45	0.106	77.81	0	8
2	5	2	9.504	0.105	78.27	49	8
0	2	4	9.514	0.105	78.38	1	4
4	4	0	9.562	0.105	78.78	1	4
5	0	1	9.587	0.104	78.95	7	4
3	5	1	9.613	0.104	79.18	28	8
1	2	4	9.694	0.103	79.87	18	8
5	1	1	9.703	0.103	79.93	16	8
2	6	0	9.727	0.103	80.10	0	4
2	0	4	9.769	0.102	80.44	1	4
2	4	3	9.779	0.102	80.56	3	8
4	3	2	9.804	0.102	80.73	65	8
4	4	1	9.825	0.102	80.90	23	8
3	3	3	9.864	0.101	81.25	1	8
2	1	4	9.883	0.101	81.42	14	8
2	6	1	9.986	0.1	82.22	6	8

hkl-Table of Fe $_3$B - tetragonal

Table 18: Crystallographic data of Fe$_3$B - tetragonal.

h	k	l	d^{-1} (nm^{-1})	d (nm)	2 Theta (°)	Intensity	Multiplicity
1	1	0	1.634	0.612	13.46	2	4
2	0	0	2.311	0.433	19.08	0	4
1	0	1	2.598	0.385	21.43	6	8
2	2	0	3.268	0.306	26.93	10	4
2	1	1	3.477	0.288	28.65	2	16
3	1	0	3.654	0.274	30.14	44	8
3	0	1	4.175	0.24	34.38	216	8
4	0	0	4.622	0.216	38.10	31	4
0	0	2	4.654	0.215	38.33	30	2
3	2	1	4.772	0.21	39.30	1000	16

3	3	0	4.902	0.204	40.39	190	4
1	1	2	4.933	0.203	40.62	467	8
4	2	0	5.167	0.194	42.57	583	8
2	0	2	5.196	0.192	42.80	113	8
4	1	1	5.302	0.189	43.66	282	16
2	2	2	5.687	0.176	46.87	132	8
5	1	0	5.891	0.17	48.53	17	8
3	1	2	5.917	0.169	48.76	493	16
5	0	1	6.228	0.161	51.28	40	8
4	3	1	6.228	0.161	51.28	32	16
4	4	0	6.536	0.153	53.86	16	4
4	0	2	6.559	0.152	54.03	32	8
5	2	1	6.643	0.151	54.72	2	16
5	3	0	6.737	0.148	55.52	28	8
3	3	2	6.76	0.148	55.69	7	8
6	0	0	6.932	0.144	57.12	1	4
4	2	2	6.954	0.144	57.30	9	16
1	0	3	7.077	0.141	58.27	12	8
6	2	0	7.307	0.137	60.22	81	8
6	1	1	7.403	0.135	60.96	7	16
2	1	3	7.444	0.134	61.31	5	16
5	1	2	7.508	0.133	61.82	29	16
5	4	1	7.756	0.129	63.88	16	16
3	0	3	7.795	0.128	64.23	36	8
4	4	2	8.024	0.125	66.12	17	8
6	3	1	8.093	0.124	66.63	124	16
3	2	3	8.13	0.123	66.98	125	16
5	5	0	8.17	0.122	67.27	41	4
7	1	0	8.17	0.122	67.27	46	8
5	3	2	8.189	0.122	67.44	298	16
6	4	0	8.332	0.12	68.64	1	8
6	0	2	8.35	0.12	68.75	21	8
7	0	1	8.416	0.119	69.33	61	8
4	1	3	8.452	0.118	69.61	65	16
6	2	2	8.664	0.115	71.33	4	16
7	2	1	8.727	0.115	71.91	122	16
7	3	0	8.799	0.114	72.48	14	8
4	3	3	9.062	0.11	74.66	51	16
5	0	3	9.062	0.11	74.66	15	8
8	0	0	9.243	0.108	76.15	0	4
0	0	4	9.309	0.107	76.66	60	2

h	k	l	d⁻¹ (nm⁻¹)	d (nm)	2 Theta (°)	Intensity	Multiplicity
6	5	1	9.319	0.107	76.78	37	16
5	2	3	9.352	0.107	77.01	20	16
5	5	2	9.403	0.106	77.46	23	8
7	1	2	9.403	0.106	77.46	87	16
1	1	4	9.451	0.106	77.86	1	8
8	2	0	9.528	0.105	78.50	0	8
6	4	2	9.544	0.105	78.61	4	16
2	0	4	9.591	0.104	79.01	3	8
8	1	1	9.601	0.104	79.07	34	16
7	4	1	9.601	0.104	79.07	40	16
6	6	0	9.804	0.102	80.73	0	4
2	2	4	9.866	0.101	81.25	2	8
6	1	3	9.906	0.101	81.59	6	16
7	5	0	9.939	0.101	81.88	9	8
7	3	2	9.954	0.1	81.99	20	16

hkl-Table of SiO$_2$

Table 19: Crystallographic data of SiO$_2$.

h	k	l	d⁻¹ (nm⁻¹)	d (nm)	2 Theta (°)	Intensity	Multiplicity
1	0	0	2.35	0.425	19.37	291	6
1	0	1	2.991	0.334	24.64	1000	12
1	1	0	4.071	0.246	33.52	130	6
1	0	2	4.384	0.228	36.10	223	12
1	1	1	4.472	0.224	36.84	60	12
2	0	0	4.701	0.213	38.73	88	6
2	0	1	5.052	0.198	41.60	123	12
1	1	2	5.501	0.182	45.32	256	12
0	0	3	5.55	0.18	45.72	1	2
2	0	2	5.982	0.167	49.27	34	12
1	0	3	6.028	0.166	49.68	8	12
2	1	0	6.218	0.161	51.22	15	12
2	1	1	6.488	0.154	53.46	116	24
1	1	3	6.883	0.145	56.72	38	12
3	0	0	7.051	0.142	58.10	10	6
2	1	2	7.236	0.138	59.59	72	24
2	0	3	7.273	0.137	59.93	244	12
3	0	1	7.29	0.137	60.05	8	12
1	0	4	7.765	0.129	63.94	89	12
3	0	2	7.963	0.126	65.60	62	12
2	2	0	8.142	0.123	67.04	25	6

2	1	3	8.335	0.12	68.64	147	24
2	2	1	8.349	0.12	68.75	19	12
1	1	4	8.446	0.118	69.56	59	12
3	1	0	8.474	0.118	69.79	68	12
3	1	1	8.674	0.115	71.45	3	24
2	0	4	8.767	0.114	72.19	15	12
2	2	2	8.943	0.112	73.68	8	12
3	0	3	8.973	0.111	73.91	14	12
3	1	2	9.247	0.108	76.15	45	24
4	0	0	9.401	0.106	77.41	4	6
1	0	5	9.545	0.105	78.61	4	12
4	0	1	9.582	0.104	78.90	52	12
2	1	4	9.666	0.103	79.64	41	24
2	2	3	9.854	0.101	81.13	16	12

B. Magnetic Characterization of the Specimens
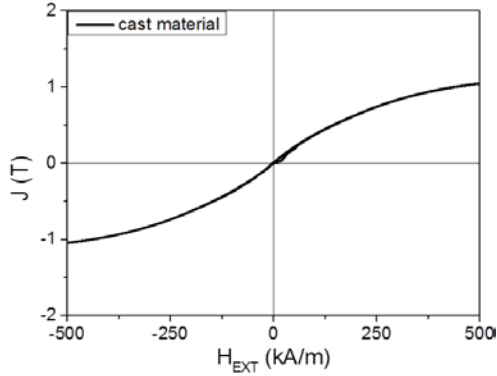
Fig. 55: Illustration of the hysteresis loop of the cast material without a response of the coercivity and weak saturation polarization.
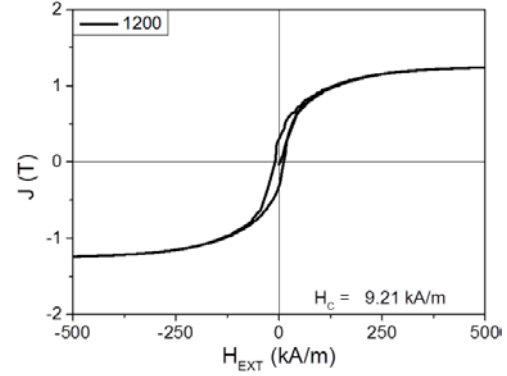
Fig. 56: The hysteresis loop of sample 1200 exhibits a coercive field of 9.21 kA/m and an increasing saturation polarization.
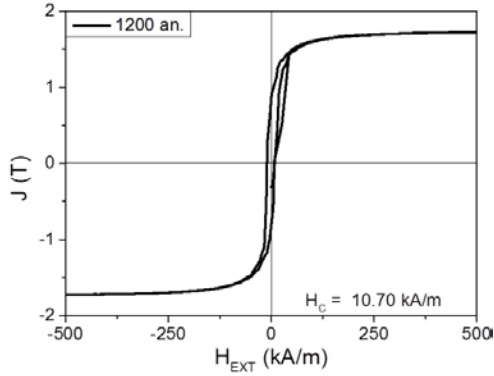
Fig. 57: The hysteresis loop of sample 1200 an. A coercivity of 10.70 kA/m and an enhancement of the saturation polarization were measured.
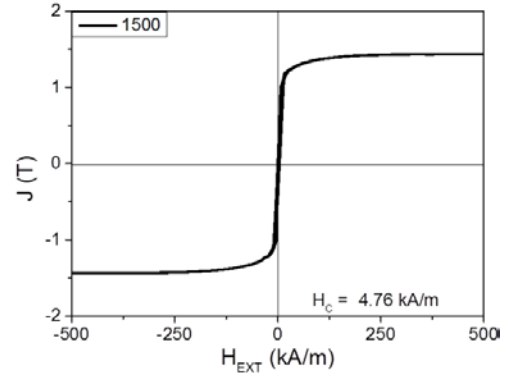
Fig. 58: Illustration of the hysteresis loop of sample 1500. Saturation polarization is increased compared to sample 1200, but coercivity is decreased.
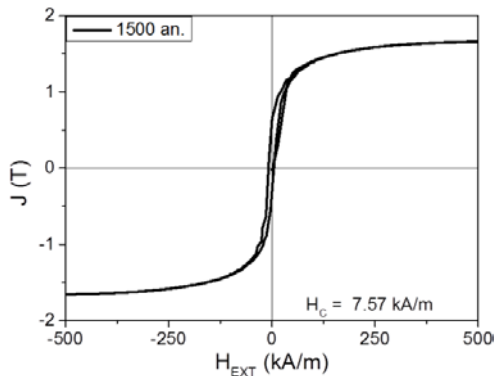
Fig. 59: The coercive field as well as the saturation polarization of sample 1500 an. are raised compared to the sample, which is not annealed.
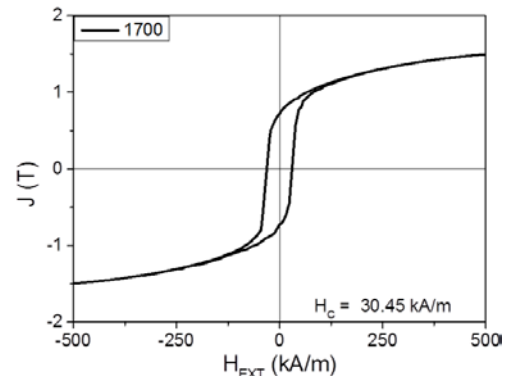
Fig. 60: Illustration of the hysteresis loop of sample 1700. A significant high value of the coercivity was measured, but the saturation polarization is slightly decreased.
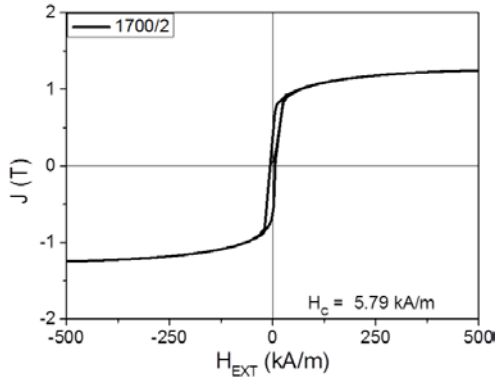
Fig. 61: The hysteresis loop of the parent alloy exhibits a weak coercivity and a weak saturation polarization.
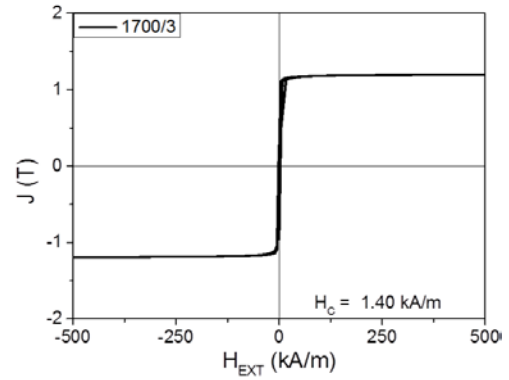
Fig. 62: The hysteresis loop of sample 1700/3 shows weak magnetic values as well as sample 1700/2.
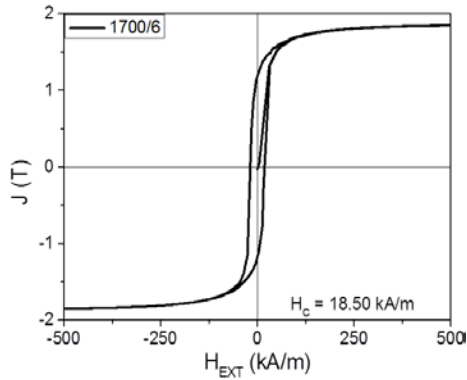
Fig. 63: Illustration of the hysteresis loop of sample 1700/6. The highest saturation polarization combined with a large coercivity was measured.
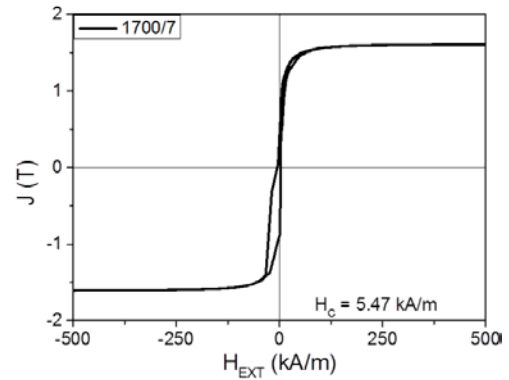
Fig. 64: The hysteresis loop of sample 1700/7 with a strong saturation polarization and a weak coercive field strength.
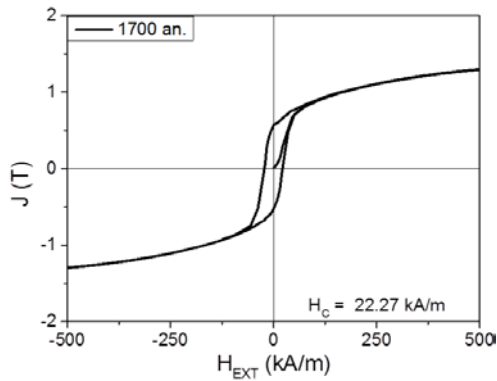
Fig. 65: The properties of sample 1700 an. are decreased compared the not annealed sample as shown in this hysteresis loop.
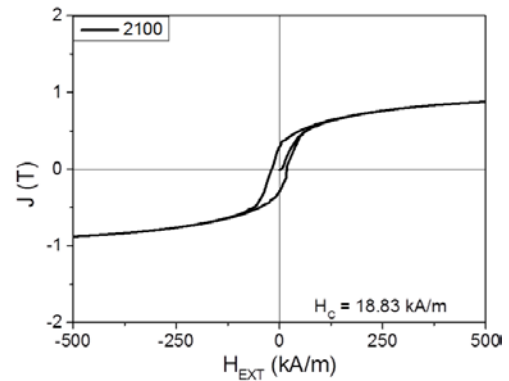
Fig. 66: Illustration of the hysteresis loop of sample 2100. The coercivity is 18.83 kA/m with a decreasing saturation polarization compared to the sample with a slower wheel speed.
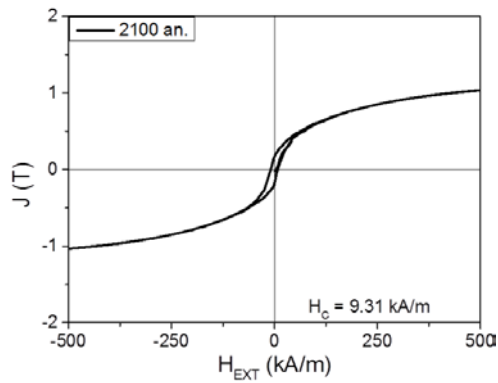
Fig. 67: The hysteresis loop of sample 2100 an. with a decreasing coercivity of 9.31 kA/m, but with an increase of the saturation polarization.
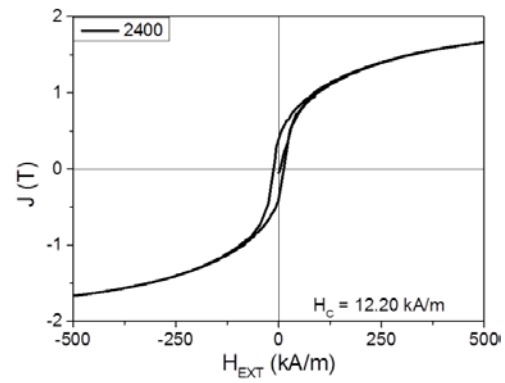
Fig. 68: Illustration of the hysteresis loop of sample 2400 with an increase in the saturation polarization and a coercivity of 12.20 kA/m.
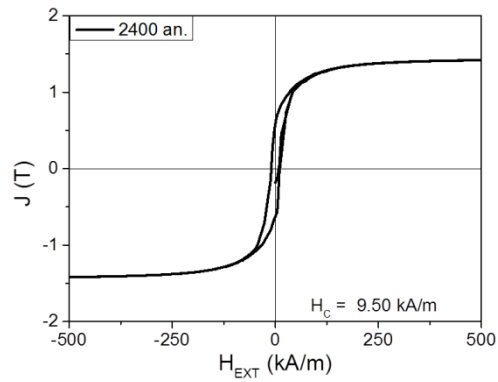
Fig. 69: Illustration of the hysteresis loop of sample 2400 an. with a coercivity of 9.50 kA/m and a weaker saturation polarization compared to the not annealed sample.

References

[1]   R. Hilzinger and W. Rodewald, *Magnetic materials*, Vacuumschmelze, 2013.

[2]   A. Kloss, *Geschichte des Magnetismus*, vde-Verlag, 1994.

[3]   J. Coey, *Magnetism and magnetic materials*, Cambridge University Press, 2010.

[4]   K.J. Buschow and F.R. de Boer, *Physics of magnetism and magnetic materials*, Springer, 2003.

[5]   D. Niarchos, *REFREEPERMAG - Rare-Earth Free Permanent Magnets,* http://refreepermag-fp7.eu/, 2014.

[6]   O. Gutfleisch, M.A. Willard, E. Brück, C.H. Chen, S. Sankar and J.P. Liu, *Magnetic materials and devices for the 21st century: stronger, lighter, and more energy efficient,* Advanced materials 237 (2011) 821-842.

[7]   J. Coey, *Permanent magnets: Plugging the gap,* Scripta Materialia 676 (2012) 524-529.

[8]   D. Goll, *Micromagnetism–Microstructure Relations and the Hysteresis Loop,* Handbook of Magnetism and Advanced Magnetic Materials, 2007.

[9]   W. Wallisch, J. Fidler, P. Toson, H. Sassik, R. Svagera and J. Bernardi, *Synthesis and Characterization of $(Fe,Co)_{2-3}B$ microcrytsalline alloys,* submitted 2015.

[10]   A. Iga, *Magnetocrystalline Anisotropy in $(Fe_{1-X}Co_X)_2B$ System,* Japanese Journal of Applied Physics 94 (1970) 415.

[11]   L. Takacs, M. Cadeville and I. Vincze, *Mossbauer study of the intermetallic compounds $(Fe_{1-X}Co_X)_2B$ and $(Fe_{1-X}Co_X)B$,* Journal of Physics F: Metal Physics 54 (1975) 800.

[12]   W. Coene, F. Hakkens, R. Coehoorn, D. De Mooij, C. De Waard, J. Fidler and R. Grössinger, *Magnetocrystalline anisotropy of Fe_3B, Fe_2B and $Fe_{1.4}Co_{0.6}B$ as studied by Lorentz electron microscopy, singular point detection and magnetization measurements,* Journal of Magnetism and Magnetic Materials 96 (1991) 189-196.

[13]   M. Kuz'min, K. Skokov, H. Jian, I. Radulov and O. Gutfleisch, *Towards high-performance permanent magnets without rare earths,* Journal of Physics: Condensed Matter 266 (2014) 064205.

[14]   H. Jian, K.P. Skokov, M.D. Kuz'min, I. Radulov and O. Gutfleisch, *Magnetic Properties of $(Fe,Co)_2B$ Alloys With Easy-Axis Anisotropy,* Magnetics, IEEE Transactions on 5011 (2014) 1-4.

[15]   K.D. Belashchenko, L. Ke, M. Däne, L.X. Benedict, T.N. Lamichhane, V. Taufour, A. Jesche, S.L. Bud'ko, P.C. Canfield and V.P. Antropov, *Origin of magnetocrystalline anisotropy in (Fe$_{1-X}$Co$_X$)$_2$B alloys,* arXiv:1501.03483 (2015).

[16]   A. Edström, M. Werwinksi, J. Rusz, O. Eriksson et. al., *Effect of doping by 5d elements on magnetic properties of (Fe$_{1-X}$Co$_X$)$_2$B alloys,* submitted 2015.

[17]   G. Bertotti, *Hysteresis in magnetism: for physicists, materials scientists, and engineers*, Academic press, 1998.

[18]   C. Kittel, *Physical theory of ferromagnetic domains,* Reviews of modern Physics 214 (1949) 541.

[19]   R. Skomski, *Simple models of magnetism*, Oxford University Press Oxford, 2008.

[20]   B.D. Cullity and C.D. Graham, *Introduction to magnetic materials*, John Wiley & Sons, 2011.

[21]   D. Suess, V. Tsiantos, T. Schrefl, J. Fidler, W. Scholz, H. Forster, R. Dittrich and J. Miles, *Time resolved micromagnetics using a preconditioned time integration method,* Journal of Magnetism and Magnetic Materials 2482 (2002) 298-311.

[22]   R. Ribó, M. Riera, E. Terceno, J. Ronda, A. Sans, A. Ribera and S. Horcas, *Gid, the personal pre and post processor*, 1997.

[23]   H. Kronmüller and M. Fähnle, *Micromagnetism and the microstructure of ferromagnetic solids,* Cambridge University Press, 2003.

[24]   J. Coey, *Hard magnetic materials: a perspective,* Magnetics, IEEE Transactions on 4712 (2011) 4671-4681.

[25]   V. Raghavan, *B-Co-Fe (Boron-Cobalt-Iron),* Journal of phase equilibria and diffusion (2012) 1-3.

[26]   P. Villars and L.D. Calvert, *Pearson's handbook of crystallographic data for intermetallic phases*, 2nd ed, ASM International, Materials Park, OH, 1991.

[27]   H. Sassik, *Probenpräparation: Herstellung von polykristallinen Proben, Einkristallen und amorphen Bändern*, in *Festkörperphysik Praktikum*.

[28]   E.H. Strange and C.A. Pim, *Process of manufacturing thin sheets, foil, strips, or ribbons of zinc, lead, or other metal or alloy*, 1908, Google Patents.

[29]   M. Calvo-Dahlborg, *Structure and embrittlement of metallic glasses,* Materials Science and Engineering: A 226 (1997) 833-845.

[30]   E. Barth, F. Spaepen, R. Bye and S. Das, *Influence of processing on the ductile-to-brittle transition temperature of an Fe-B-Si metallic glass,* Acta materialia 451 (1997) 423-428.

[31] V.I. Tkatch, A.I. Limanovskii, S.N. Denisenko and S.G. Rassolov, *The effect of the melt-spinning processing parameters on the rate of cooling,* Materials Science and Engineering: A 3231 (2002) 91-96.

[32] S. Takayama and T. Oi, *The analysis of casting conditions of amorphous alloys,* Journal of Applied Physics 507 (1979) 4962-4965.

[33] C. Graham Jr and T. Egami, *Magnetic properties of amorphous alloys,* Annual Review of Materials Science 81 (1978) 423-457.

[34] H.-J. Bargel and G. Schulze, *Werkstoffkunde*, 11., bearb. Aufl. ed, Springer Berlin Heidelberg Berlin, 2012.

[35] L. Spieß, G. Teichert, R. Schwarzer, H. Behnken and C. Genzel, *Moderne Röntgenbeugung,* Vieweg+ Teubner (2009).

[36] K. Momma and F. Izumi, *VESTA 3 for three-dimensional visualization of crystal, volumetric and morphology data,* Journal of Applied Crystallography 446 (2011) 1272-1276.

[37] P. Stadelmann, *JEMS-EMS java version,* CIME-EPFL, Lausanne, Switzerland, 2004.

[38] W. Kraus and G. Nolze, *POWDER CELL–a program for the representation and manipulation of crystal structures and calculation of the resulting X-ray powder patterns,* Journal of Applied Crystallography 293 (1996) 301-303.

[39] D. Williams and C.B. Carter, *The Transmission Electron Microscope*, in *Transmission Electron Microscopy*, Springer US, 1996.

[40] M. Knoll and E. Ruska, *Das Elektronenmikroskop,* Z. Physik 785-6 (1932) 318-339.

[41] R. Erni, M.D. Rossell, C. Kisielowski and U. Dahmen, *Atomic-resolution imaging with a sub-50-pm electron probe,* Physical Review Letters 1029 (2009) 096101.

[42] M. von Heimendahl, *Einführung in die Elektronenmikroskopie*, Vieweg Braunschweig, 1970.

[43] J. Fidler, *Grundlagen der Elektronenmikroskopie*. Vorlesungsskriptum VO 133.293, Vol. 5.0. Institute of Solid State Physic,Vienna University of Technology

[44] B. Schaefer and H.N.L. der Experimentalphysik, *Band 3: Optik, 10,* Auflage de Gruyter Verlag, Berlin, 2004.

List of Figures

List of Tables

Publications

P. Toson, W. Wallisch, A. Asali, J. Fidler:
"*Modelling of Packed Co Nanorods for Hard Magnetic Applications*";
EPJ Web of Conferences, 75 (JEMS 2013 - Joint European Magnetic Symposia (2014), 03002.

V. Alexandrakis, W. Wallisch, S. Hamann, G. Varvaro, J. Fidler, A. Ludwig:
"*Combinatorial Development of Fe-Co-Nb Thin Film Magnetic Nanocomposites*";
Submitted

G.Giannopoulos, L. Reichel, A. Markou, W. Wallisch, M. Stöger-Pollach, I. Panagiotopoulos,
V. Psycharis, S. Fähler, J. Fidler and D. Niarchos:
"*Structural and magnetic properties of strongly carbon doped Fe-Co thin films*";
Submitted

W. Wallisch, J. Fidler, P. Toson, H. Sassik, R. Svagera and J. Bernardi:
"*Synthesis and characterization of $(Fe,Co)_{2-3}B$ microcrystalline alloys* ";
Submitted

Presentations

W. Wallisch, P. Toson, A. Asali, H. Sassik, J. Fidler:
"*Synthesis and analysis of (Fe,Co)2-3B microcrystalline alloys*";
Talk: JEMS 2013, Joint European Magnetic Symposia, Rhodes, Greece; 2013-08-25 -
2013-08-30.

P. Toson, A. Asali, W. Wallisch, J. Fidler:
"*Simulation of hysteresis properties of realistically packed nanorod structures*";
Talk: JEMS 2013, Joint European Magnetic Symposia, Rhodes, Greece; 2013-08-25 –
2013-08-30.

W. Wallisch, G. A. Zickler, M. Stöger-Pollach, J. Bernardi, J. Fidler:
"*Analytical TEM investigations of (Fe,Co)$_{2-3}$B microcrystalline alloys*";
Poster: 4th ASEM-Workshop, University of Vienna; 2014-05-08 - 2014-05-09;
in: "*4th ASEM-Workshop on Advanced Electron Microscopy*", (2014).

G. A. Zickler, K. Zagar, W. Wallisch, M. Stöger-Pollach, J. Bernardi, J. Fidler:
"*Nanoanalytical TEM/STEM methods for the characterisation of grain boundary phases from rare earth permanent magnets*";
Poster: 4th ASEM-Workshop, University of Vienna; 2014-05-08 - 2014-05-09;
in: "*4th ASEM-Workshop on Advanced Electron Microscopy*", (2014).

G. Giannopoulos, L. Reichel, A. Markou, S. Kauffmann-Weiß, I. Panagiotopoulos, K. Mergia, V. Psycharis, A. Lagogiannis, A. Edström, W. Wallisch, E. Delczeg, M. Werwinski, J. Rusz, S. Fähler, J. Fidler, D. Niarchos:
"*Structural and magnetic properties of strongly carbon doped Fe-Co thin films*";
Poster: IEEE Int. Magnetics Conference (Intermag 2014), Dresden, Germany; 2014-05-04 -
2014-05-08.

P. Toson, A. Asali, W. Wallisch, G. A. Zickler, J. Fidler:
"*Nanostructured Hard Magnets: A Micromagnetic Study*";
Poster: 10th European Conference on Magnetic Sensors and Actuators (EMSA 2014), Vienna, Austria; 2014-07-04 - 2014-07-09.

G. Giannopoulos, C. Sarafidis, M. Gjoka, L. Reichel, A. Markou, W. Wallisch, V. Psycharis, J. Fidler, D. Niarchos:
"*Rare Earth Free Permanent Magnets*";
Talk: REPM2014 - Rare Earth and Future Permanent Magnets and Their Applications Workshop 2014, Annapolis, USA; 2014-08-17 - 2014-08-21.

W. Wallisch, M. Stöger-Pollach, G. A. Zickler, G. Giannopoulos, D. Niarchos, J. Fidler:
"*EMCD-investigation of Co-Fe thin films doped with carbon by Analytical TEM*";
Poster: 18th International Microscopy Congress, Prague; 2014-09-07 - 2014-09-12;

in: "*18th International Microscopy Congress Proceedings*", Czechoslovak Microscopy Society, (2014), ISBN: 978-80-260-6720-7; Paper ID MS-12-P-2050, 2 pages.

G. A. Zickler, W. Wallisch, M. Stöger-Pollach, J. Bernardi, K. Üstüner, J. Fidler:
"*TEM investigation of grain boundaries from Nd$_2$Fe$_{14}$B hard magnets*";
Poster: 18th International Microscopy Congress, Prague; 2014-09-07 - 2014-09-12;
in: "*18th International Microscopy Congress Proceedings*", Czechoslovak Microscopy Society, (2014), ISBN: 978-80-260-6720-7; Paper ID MS-12-P-1643, 2 pages.

W. Wallisch, M. Stöger-Pollach, G. Giannopoulos, S. Löffler, D. Niarchos, J. Fidler:
"*Energy loss magnetic chiral dichroism analysis of carbon doped Co-Fe thin films*";
Poster: European Workshop on Quantitative STEM Imaging, EELS and EDXS (AdSTEM 2014), Piran, Slovenia; 2014-09-29 - 2014-10-03.

Curriculum Vitae

Name:	Wolfgang Wallisch
Date of birth:	27.09.1987
Place of birth:	Vienna
Nationality:	Austrian
Address:	Hackengasse 7/23, 1150 Wien, Austria

09/2014	Attendance at the European Workshop on Quantitative STEM Imaging, EELS and EDXS (AdSTEM 2014), Piran, Slovenia.
09/2014	Attendance at the 18th International Microscopy Congress, Prague, Czech Republic.
05/2014	Attendance at the 4th ASEM-Workshop on Advanced Electron Microscopy, University of Vienna, Austria.
04/2014	The project Rare-Earth Free Permanent Magnets (REFREEPERMAG) received an award as one of the "Best on-going Project" in FP7 of the EU.
08/2013	Attendance at the JEMS Joint European Magnetic Symposia 2013, Rhodes, Greece.
02/2013	Attendance at the ViCoM Winter School "Phase stability and phase transitions on soft and hard materials", St. Christoph, Austria.
From 11/2012	Research assistant in the research group of J. Fidler at the Institute of Solid State Physics, Vienna University of Technology. In an EU-NMP funded project "Rare-Earth Free Permanent Magnets" (REFREEPERMAG), which is concerned with the development of a new generation of high-performance permanent magnets without rare-earths.
From 11/2012	Master program in Technical Physics, Vienna University of Technology.
10/2012	Bachelor degree in Technical Physics, Vienna University of Technology, "Preparation and TEM-investigation of (FePt) multilayer systems".
07/2012 - 10/2012	Student assistant in the research group of J. Fidler at the Institute of Solid State Physics, Vienna University of Technology.
07/2011 - 12/2011	Student assistant in the research group of J. Fidler at the Institute of Solid State Physics, Vienna University of Technology.
09/2009 - 05/2013	Diverse student jobs.
10/2007 - 10/2012	Bachelor program in Technical Physics, Vienna University of Technology.
09/2006 - 02/2007	Basic military service (Präsenzdienst).
06/2006	Matura (school leaving examination), Vienna.